nature chemistry

Article

https://doi.org/10.1038/s41557-023-01267-1

Kinetic control of shape deformations and membrane phase separation inside giant vesicles

Received: 19 August 2021

Accepted: 6 June 2023

Published online: 6 July 2023

Check for updates

Wan-Chih Su[1], James C. S. Ho[2], Douglas L. Gettel[3], Andrew T. Rowland[4], Christine D. Keating[4] ✉ & Atul N. Parikh[1,2,3,5] ✉

A variety of cellular processes use liquid–liquid phase separation (LLPS) to create functional levels of organization, but the kinetic pathways by which it proceeds remain incompletely understood. Here in real time, we monitor the dynamics of LLPS of mixtures of segregatively phase-separating polymers inside all-synthetic, giant unilamellar vesicles. After dynamically triggering phase separation, we find that the ensuing relaxation—en route to the new equilibrium—is non-trivially modulated by a dynamic interplay between the coarsening of the evolving droplet phase and the interactive membrane boundary. The membrane boundary is preferentially wetted by one of the incipient phases, dynamically arresting the progression of coarsening and deforming the membrane. When the vesicles are composed of phase-separating mixtures of common lipids, LLPS within the vesicular interior becomes coupled to the membrane's compositional degrees of freedom, producing microphase-separated membrane textures. This coupling of bulk and surface phase-separation processes suggests a physical principle by which LLPS inside living cells might be dynamically regulated and communicated to the cellular boundaries.

When a binary fluid mixture is quenched from a uniform homogeneous phase into the coexistence region, it enters into a far-from-equilibrium state[1,2]. Subsequent evolution of this non-equilibrium system—in which the disordered 'mother' phase gives way to new coexisting phases at equilibrium—is not instantaneous. Instead, complementary regions of the new broken-symmetry phases grow and coarsen over time. Here, growth corresponds to an increase in the volume fraction of the droplet phase via the transport of molecules from the complementary matrix phase. Coarsening, which follows growth, represents morphological evolution due to changes in droplet size at the fixed, equilibrated value of the volume fraction[3]. In both cases, the kinetic pathways of phase separation are determined by material transport through a combination of diffusion- and flow-mediated mechanisms, ultimately producing phase-separated morphologies of droplets enriched in either component. This general phenomenology of phase-ordering governs the evolution of compositional patterns during phase separation, dictating equilibrium textures of phase-separated systems across many disparate classes of material, including metal alloys, magnetic solids, polymers, colloids and liquid crystals[3].

However, all material systems undergo phase separation within finite containers. The physical limits that the container boundaries impose—including finite system size and the proximity of the bounding surface—introduce new constraints that influence phase separation, perturb diffusive and hydrodynamic processes, and alter morphological evolution[4]. Consider, for example, a surface that preferentially wets one of the incipient coexisting phases over the other—this spatially

[1]Chemistry Graduate Program, University of California, Davis, CA, USA. [2]Singapore Centre for Environmental Life Sciences Engineering and Institute for Digital Molecular Analytics and Science, Nanyang Technological University, Nanyang Technological University, Singapore, Singapore. [3]Chemical Engineering Graduate Program, University of California, Davis, CA, USA. [4]Department of Chemistry, The Pennsylvania State University, University Park, PA, USA. [5]Biomedical Engineering Graduate Programs, University of California, Davis, CA, USA. ✉e-mail: cmd8@psu.edu; anparikh@ucdavis.edu

patterns the two phases, altering the course and kinetics of phase separation and influencing morphological evolution[5,6]. This phenomenon of surface-directed spinodal decomposition is perhaps best exemplified by studies of polymer mixtures undergoing liquid–liquid phase separation (LLPS). These studies document a rich variety of ways by which solid surfaces intervene in the dynamics of phase separation. Examples include the formation of compositional waves near the surface[7], acceleration of domain coarsening[8,9] and the emergence of double phase separation[10].

These behaviours are of particular interest in soft matter and biological systems undergoing LLPS, such as aqueous solutions of proteins and polymers in biological (cellular and subcellular) and synthetic (vesicular) compartments[11]. Here, phase separation proceeds in physically confined (femto- to picolitre quantities) and macromolecularly crowded volumes within topologically closed compartments[12,13]. Moreover, the compartmental boundaries (membranes) are neither passive nor non-responsive—they are fluid, deformable and molecularly heterogeneous, and are capable of interacting differentially with the incipient phases. This range of system attributes, namely, surface wetting, spatial confinement, surface deformability and membrane composition, influence LLPS in complex ways, setting the stage for rich and complex phase behaviours in confined soft-matter and biological systems. A number of recent studies have sought to explore these relations between the membrane boundary and phase-separated states[14–17]. Among these, a recent example that demonstrated the phase behaviour of the bacterial nucleoid occlusion protein Noc is particularly noteworthy. An in vitro reconstitution reveals how droplets of Noc condensates formed upon cytidine triphosphate binding interact with and deform the membrane and conversely how membrane characteristics influence condensate formation[17]. None of these studies, however, have focused on the real-time, dynamic characterization of how an incipient LLPS influences the membrane boundary and, conversely, how the proximal boundary alters the course of phase separation.

In considering real-time phase separation under the global constraints of vesicular confinement, several general questions naturally arise. (1) Are growth and phase coarsening limited to the intravesicular bulk or may the surface direct LLPS? (2) How are the kinetics influenced by the system size, geometry and proximity of the membrane surface? (3) Might preferential wetting by the droplets, which locally deforms the membrane, spatially reorganize the membrane components, thereby coupling LLPS within the vesicular bulk (three-dimensional (3D)) with the lipid–lipid phase separation (two-dimensional (2D)) within the membrane? (4) Does the interplay between phase separation and wetting arrest the relaxation of the coarsening system into a metastable minimum instead of the true thermodynamic ground state?

Addressing these questions is particularly timely[11] given the rapidly growing recognition of the prevalence of LLPS across biology and its purported role as a driver for the formation of biomolecular condensates—a critical level of functional organization within a living cell[18–21]. Indeed, a growing body of recent observations suggest that there is a complex interplay between intracellular LLPS and membrane assembly at cellular boundaries[15,22,23]. The cellular context of many diverse classes of LLPS investigated so far has focused on associative phase separation—weak, non-covalent and often multivalent attractive interactions between biomacromolecules (nucleic acids and proteins generally containing low-complexity domains) producing coexisting phases of protein- (and nucleic acid-) enriched droplet condensates dispersed in protein-depleted surroundings. However, the scope of LLPS in the biological context is unlikely to be limited to attractive interactions alone. This is because many associative LLPS processes occur in macromolecularly crowded cytoplasmic space, which introduces segregative phase separation through excluded volume interactions and depletion forces[24]. Indeed, many of the recently discovered, associative LLPS processes are now known to proceed more robustly and at lower concentrations in crowded environments[24,25]. Thus, it seems clear that the full scope of LLPS-mediated processes in biological and synthetic contexts would require considerations of how the crowded space textured by segregative phase separation modulates associative phase separation.

Results and discussion

In this Article, we experimentally investigate a model case of phase-ordering inside single vesicular compartments in situ. The phase-ordering system we employ is a minimal aqueous two-phase system (ATPS) consisting of aqueous mixtures of two chemically dissimilar and electrically neutral polymers: polyethylene glycol (PEG) and dextran[26]. First developed for biomolecular separations, the ATPS system of PEG and dextran is segregative[26]. At low weight fractions, these mixtures adopt a single homogeneous phase. Beyond a threshold concentration, they phase-separate, producing two coexisting phases at equilibrium, with each phase enriching a different polymer. A binodal line dividing the two regions characterizes the phase diagram of these mixtures[26].

Our vesicular compartments, which encapsulate the ATPS components in an initially homogeneous phase, are giant unilamellar vesicles (GUVs)[27]. These are the simplest, cell-sized (radius r of ~5–50 μm), topologically closed and nominally spherical synthetic compartments, and they isolate picolitre quantities of the encapsulated aqueous phase from the surrounding bulk. The GUVs are bounded by a 2D, fluid, highly deformable and water-permeable ($P_{water} \approx 10^{-3}$ cm s^{-1}) but solute-impermeable ($P_{solute} \approx 10^{-8}$–$10^{-10}$ cm s^{-1}) bilayer lipid membrane[28]. To induce LLPS in real time, we subjected the GUVs to an abrupt hypertonic stress, which, by rapidly expelling water from the intravesicular lumen (characteristic permeation time, $r/3P_{water} = (10 \times 10^{-4})/(3 \times 10^{-3}) \approx 0.3$ s, abruptly elevates the polymer concentrations and quenches the mixtures inside the coexistence curve (Fig. 1a). Methods for the encapsulation of the ATPS components within vesicular compartments[29,30] and their osmotically mediated phase separation[31–33] are well-established in recent literature. The use of aqueous-phase separation inside vesicular compartments was first developed[29,30] to minimally recapitulate the physical features of cytosolic micro-compartmentation, such as that which occurs in living cells[34,35]. Since these early demonstrations, many studies have explored the equilibrium behaviours of ATPS-encapsulating GUVs. In a series of studies, Dimova, Lipowsky and others have investigated how equilibrated droplets interact with the bounding membrane[36,37]. These efforts established the role of surface wetting, which, together with membrane mechanics, offers important insights and quantitative explanations of the features of equilibrium morphologies, namely droplet-induced budding and membrane tubulation arising from LLPS.

We began by preparing GUVs using the standard electroformation technique[38]. For single-component GUVs we used monounsaturated phospholipid, namely 1-palmitoyl-2-oleoyl-*sn*-1-glycero-3-phosphocholine (POPC), and our ternary GUVs included predetermined mixtures containing POPC, cholesterol (Ch) and sphingomyelin (SM). Depending on the composition, temperature, membrane tension and solution conditions, the latter mixture forms a single uniform phase or exhibits microscopic phase separation, with the latter characterized by two coexisting liquid phases: a dense phase enriched in SM and Ch designated as the L_o (liquid-ordered) phase and a second, less-dense L_d (liquid-disordered) phase consisting primarily of POPC[39]. In both cases, we introduced a small concentration of methoxy PEG derivatized 1,2-dioleoyl-*sn*-glycero-3-phosphatidylethanolamine (DOPE-mPEG 2000, 2.2 mol%) or monosialoganglioside (GM1, 4 mol%), which are known to facilitate the reproducible formation of GUVs[40] (Methods). To enable visualization of the membrane by fluorescence microscopy, the GUVs were spiked with a small concentration (1.0 mol%) of a probe lipid, namely 1,2-dioleoyl-*sn*-glycero-3-phosphoethanolamine-*N*-(lissamine rhodamine B sulfonyl) (Rho-DOPE). In selected experiments employing phase-separating lipid mixtures,

https://doi.org/10.1038/s41557-023-01267-1

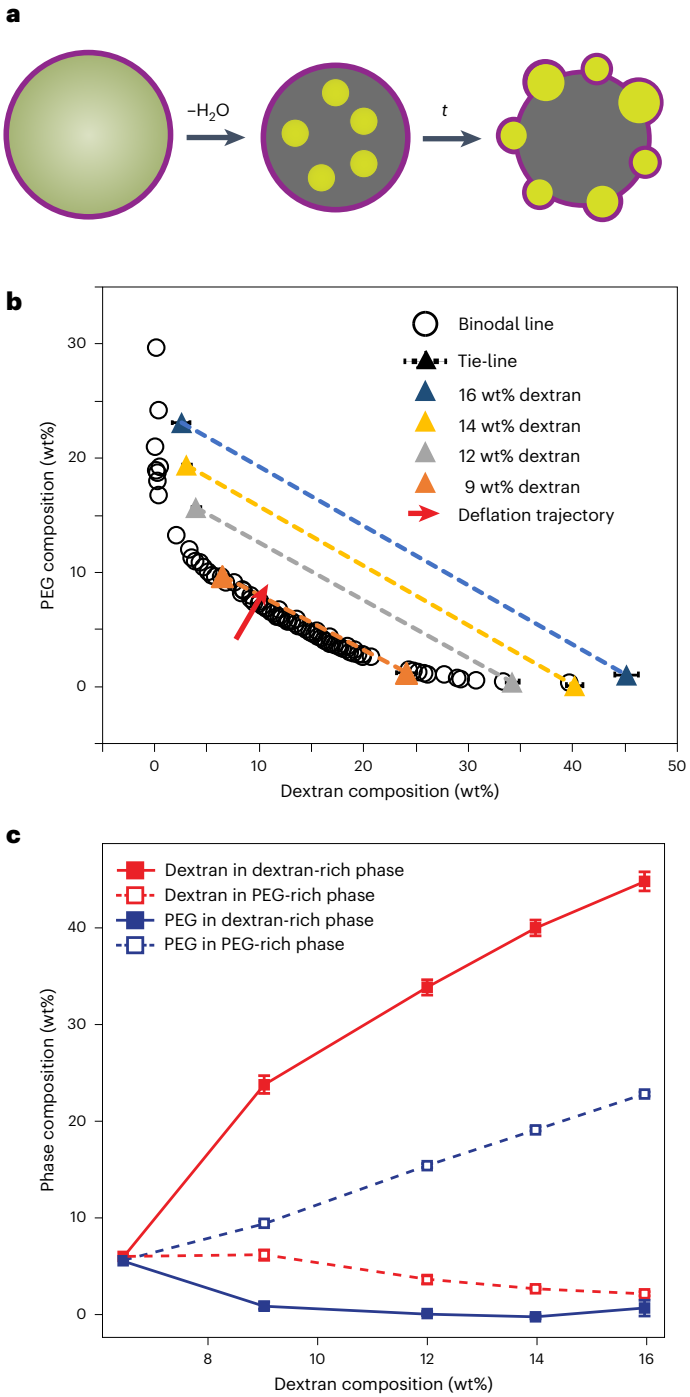

Fig. 1 | Segregative phase separation of PEG and dextran. a, Schematic of the osmotic deswelling process for inducing LLPS in situ. **b**, Binodal and tie-lines of PEG (8 kDa) and dextran (10 kDa) at room temperature. The binodal line is obtained by the cloud-point method in bulk solution. Tie-lines are obtained from the phase compositions of the PEG-rich and dextran-rich phases. The dextran concentrations of the initial solutions (for a PEG/dextran wt ratio of 15/16) are (1) 16 wt% (blue); (2) 14 wt% (yellow); (3) 12 wt% (grey); (4) 9 wt% (orange). The endpoints of the tie-lines represent the composition of the PEG-rich phase (upper left point) and dextran-rich phase (lower right point). **c**, Measurement of the phase composition of polymers in the PEG-rich and dextran-rich phases. Data are presented as mean values ± s.d.; $n = 3$, where n is the number of GUVs measured.

we also used a second fluorescent probe, 1,2-dioleoyl-*sn*-glycero-3-phosphoethanolamine-*N*-(7-nitro-2-1,3-benzoxadiazol-4-yl) (ammonium salt) (NBD-PE, 3 mol%), which exhibits a greater preference for partitioning into the liquid-ordered phase[41]. To encapsulate the ATPS inside GUVs, we used aqueous solutions containing mixtures of PEG (8 kDa) and dextran (10 kDa)[34] (Supplementary Table 1) during the hydration step of electroformation. In all cases, we chose initial concentrations that exist as a single homogeneous phase. As a guide, we used the binodal phase diagram of their bulk solutions, which we determined using standard cloud-point determination[42] (Fig. 1b and Supplementary Fig. 1). Note that the actual ATPS compositions inside individual GUVs often display vesicle-to-vesicle variability within a population. These variabilities are evident in the differences in relative phase volumes.

Substituting the extravesicular dispersion medium with an aqueous phase containing osmotically active sucrose (100–300 mM) produces a hypertonic bath, subjecting the GUV to a trans-bilayer osmotic gradient. The accompanying osmotic efflux of water from the vesicular interior elevates the concentrations of PEG and dextran polymers in the GUV interior above the binodal line, triggering phase separation in situ (Fig. 1a). The new coexisting phases formed upon hyperosmotic stress differ in their composition and density and thus viscosity and refractive index. Bulk assays confirm that the dextran-rich phase is denser and displays a higher refractive index[26]. Combining bulk polarimetric measurements with refractometry measurements allows for an initial assessment of phase compositions: for each of the two coexisting phases, the former estimates dextran concentration from optical rotation data and the latter measures total polymer concentration in each of the two phases. The two molecular compositions correspond to the endpoints of the tie-lines and quantify the fractionation of the two polymers between the coexisting phases. The results summarized in Fig. 1c confirm efficient sorting, especially at higher dextran concentrations: the PEG-rich phase contains vanishing concentrations of dextran and conversely the dextran-rich phase has only a small concentration of PEG. These observations also confirm that the total polymer loading in the dextran-rich phase is considerably higher than in the PEG-rich phase, consistent with the greater density of the dextran-rich phase.

Monitoring the dynamics of phase separation using spinning disc confocal and wide-field fluorescence microscopy documents the phase transition trajectory. A selection of images from time-lapse movies (Supplementary Videos 1 and 2) is shown in Fig. 2a–e following immersion of a representative suspension of quasi-single-component GUVs (~97% POPC) formed in a solution containing 6 wt% PEG (8 kDa) and 6.4 wt% dextran (10 kDa) in the surrounding bath containing 143 mM sucrose. Based on the bulk measurements, the osmotic pressure of the polymer mixture containing 6 wt% PEG (8 kDa) and 6.4 wt% dextran (10 kDa) corresponds to ~70 mM sucrose. Thus, immersion into 143 mM sucrose-laden bath subjects the GUV population to a net hypertonic stress ($\Delta\Pi = RT\Delta c \approx 0.1$ MPa, where R is the gas constant, T is the absolute temperature, and Δc is the molar concentration difference between the interior and exterior of the GUV), which expels water from the vesicular interior and elevates the polymer concentrations (Supplementary Table 1).

Time-lapse fluorescence images reveal a sequence of four well-differentiated kinetic regimes, described in turn in the following. First, within tens of seconds after subjecting the GUV to hyperosmotic stress ($t = 0$ corresponds to the instance when GUVs are immersed in the hypertonic bath), tubular protrusions directed toward the interior of the vesicles become visible (Fig. 2a,e). This appearance of localized tubular invaginations (in response to the reduction of the enclosed volume for a fixed membrane area, which ensues because of osmotic removal of water) at first appears counterintuitive. It is at variance with the theoretically expected shape diagrams predicting increased membrane fluctuations and well-defined global shape changes, which characterize the equilibrium configurations for various reduced volumes[43]. It, however, confirms similar findings reported previously[32,37,44] and lends support to the notion that the tubular protrusions are generated by in situ changes and stabilized kinetically.

Second, over the next several hundreds of seconds (150 s < t < 400 s), the dextran-rich droplets suspended within the vesicular lumen display a gradual increase in the fluorescence intensity (due to the labelled dextran) and grow in size (and polydispersity) (Fig. 2a,b). The former is consistent with droplet growth via diffusive transport, and the latter reflects coarsening (Fig. 2f,g, Extended Data Figs. 1 and 2 and Supplementary Fig. 2). Monitoring the changes in the fluorescence intensity (due to labelled dextran) of the droplets and the surrounding phase during this regime reveals that the mean fluorescence intensity for all droplets continues to increase with time until reaching an asymptotic intensity (~10 min). Quantifying the dextran partition coefficient (K), defined as the ratio of dextran in the PEG-rich phase to dextran in the dextran-rich phase, we estimate the asymptotic partition K to be ~0.5 (Fig. 2f, inset), which is in good agreement with that observed for the bulk solution, and those reported previously[34].

Third, at ~250 s (Fig. 2a), we find that the coalescence of some of the droplets is abruptly interrupted. Instead of indefinite droplet growth culminating in macroscopic phase separation, we find that the extant droplets, which were initially suspended within the vesicular interior, begin to accumulate at (and adhere to) the membrane surface. Over time (~400 s), most if not all droplets adhere to the membrane boundary. We also find that some (not all) of the droplets become wrapped by the tubular invaginations (Fig. 2c–e and Extended Data Figs. 3 and 4) that formed during the first regime. In both cases, this partial 'emulsification' of the droplets by the membrane appears to be a key event for understanding the kinetic arrest of droplet coarsening. For all peripheral droplets bound to the vesicular boundary, the droplet mobilities are confined to the surface and strongly suppressed. Moreover, many of the membrane-deforming droplets are decorated by surface-adsorbed tubules (Fig. 2a,e), which act as a barrier against droplet coalescence. Together, these constraints serve to arrest coarsening, leading to a metastable multi-droplet organization. Such dynamic arrests are common in many phase-separating systems, including colloids, gels and concentrated protein solutions, but they typically arise when one of the phase-separating components gels or vitrifies, producing non-equilibrium metastable states[45]. In the present case, the dynamic arrest produces a rather unusual scenario: the morphological evolution emanating from an unstable quench gives rise to metastable spatial organization of putative equilibrium phases[46]—the latter confirmed by the observations of comparable intensities (within 4%) of bound droplets.

The droplets grow by a combination of at least two independent mechanisms (Fig. 2g): (1) evaporation-condensation and (2) Brownian coagulation. In the former, the growth of larger droplets at the expense of smaller droplets is driven by the translational diffusive flux from the smaller to the larger droplets via the Lifshitz–Slyozov–Wagner mechanism, akin to Ostwald ripening. In the latter mechanism, coarsening proceeds through collisions and coalescence of droplets undergoing stochastic Brownian motion[47,48]. In both cases, the growth-coarsening rate follows a power-law dependence[1,49] consistent with the generalized $R(t) \propto t^{\alpha}$ form with a growth exponent of $\alpha = 1/3$ (refs. 50,51). Analysing the growth-coarsening rate of the droplets in our experiments, we find the power-law dependence[1,49], but with an exponent α of ~0.8(±0.2) (n = 10; Fig. 2h,i, Extended Data Fig. 5 and Supplementary Fig. 3).

The kinetic acceleration we observe may reflect the roles the proximal surface and the spatial confinements play in modulating transport processes. Previous studies of surface-directed spinodal decomposition of polymer mixtures near surfaces[5,8] have reported higher growth rates ($\alpha = 3/2$) and attributed them to surface effects[9,52]. In our case, the dextran-rich droplets almost invariably appear, grow and coarsen deep within the vesicular lumen, away from the bounding membrane, with the latter remaining fully wetted by the PEG-enriched majority phase during this regime. Thus, the presence of the proximal surface might influence the coarsening dynamics indirectly by effectively depleting dextran and the droplets from the bounding membrane, which remain wetted by PEG. It can thus increase the effective dextran and droplet concentrations, which might explain the apparent acceleration in coalescence kinetics.

Fourth, upon wetting the membrane surface, the dextran-rich droplets deform the wetted area, producing a striking mosaic of outwardly directed buds, which remain in contiguity with the mother vesicle (Fig. 2d). These buds thus provide specialized niches to spatially organize intravesicular aqueous phases and divide the otherwise contiguous membrane of nominally single composition into distinct segments with different curvatures and mechanical tensions. The sizes (and the numbers) of the buds correspond to those of individual droplets formed at the onset of membrane wetting at $t \approx 250$ s. Although similar in appearance, this droplet-induced budding is distinctly different from the budding transitions in phase-separated membranes[53,54].

From a mechanics-energetics point of view, the domain-induced budding is determined by the balance of the line tension σ that exists at the domain boundary and the curvature energy κ—both determined by the membrane's internal compositional degrees of freedom. Above a characteristic length, $l \cong \kappa/\sigma$, deformation of an initially flat domain producing buds is energetically favoured[54]. Using typical values of $\kappa \approx 10^{-19}$ J and $\sigma \approx 10^{-11}$–10^{-12} N then estimates the critical threshold of 10–100 nm for the hemispherical bud to form. In contrast, the energetic driver for the droplet-induced budding has an extrinsic origin: the interfacial tension between the coexisting aqueous phases, namely dextran-rich droplets and the PEG-rich surrounding, which does not depend on the membrane properties. Here, the competition between the corresponding interfacial energy $\Sigma_{pd} \times A_{pd}$ and the curvature energy sets the characteristic length scale at $\sqrt{\kappa/\Sigma_{pd}}$. Using the typical values of $\kappa \sim 10^{-19}$ J and our previous estimate of $\Sigma_{pd} \sim 0.36 \times 10^{-3}$ N m^{-1} (ref. 55) for comparable compositions suggests that, here too, budding is favoured beyond the nanometre-scale droplet size of ~10 nm. Moreover, because the aqueous-phase interfacial tension can be tuned by changing polymer types, concentrations and molecular weights[36], droplet-induced budding morphologies do not require the presence of materially different membrane domains.

Next, it is notable that the bud shapes, sizes and numbers do not change for several hours (~4 h). Examining the evolution of the bud morphology over the long term (>24 h) reveals a slow coarsening that ultimately replaces the multi-budded GUV configuration with one characterized by a single bud (Extended Data Fig. 6), such as expected at equilibrium[37]. This dramatic slow down in the coarsening of membrane-bound dextran-rich droplets parallels the similarly slow coarsening dynamics of domain-induced buds[56–59]: as two membrane-bound droplets that locally deform the membrane approach one another, the membrane segment ('skirt' region) between the droplets is also deformed (Fig. 2c and Supplementary Fig. 3). It is known that when the buds are within the ranges of their elastic decay lengths, this deformation of the skirt region gives rise to a net inter-bud repulsive force and elevates the activation energy barrier for bud coalescence[57,58,60]. This reasoning then suggests that the elastic properties of the membrane can arrest the droplet coarsening—a direct consequence of preferential interactions between the membrane and phase-separated droplets. Another consequence of this short length-scale inter-bud repulsion is that it can spatially organize membrane domains, producing higher-order superlattice patterns. Although the polydispersity of buds and our measurement methods are not readily amenable to detailed quantitative characterization, we often observe a relatively monodisperse population of buds that organize into extended quasi-ordered 2D lattices (Supplementary Fig. 4).

These osmotically induced LLPS and accompanying membrane deformations are fully reversible, although the reversal kinetics are different. On lowering the sucrose concentration in the bath close to the starting isotonic value, the phase-separated interior of the budded GUVs abruptly transitions to the single homogeneous phase and the

https://doi.org/10.1038/s41557-023-01267-1

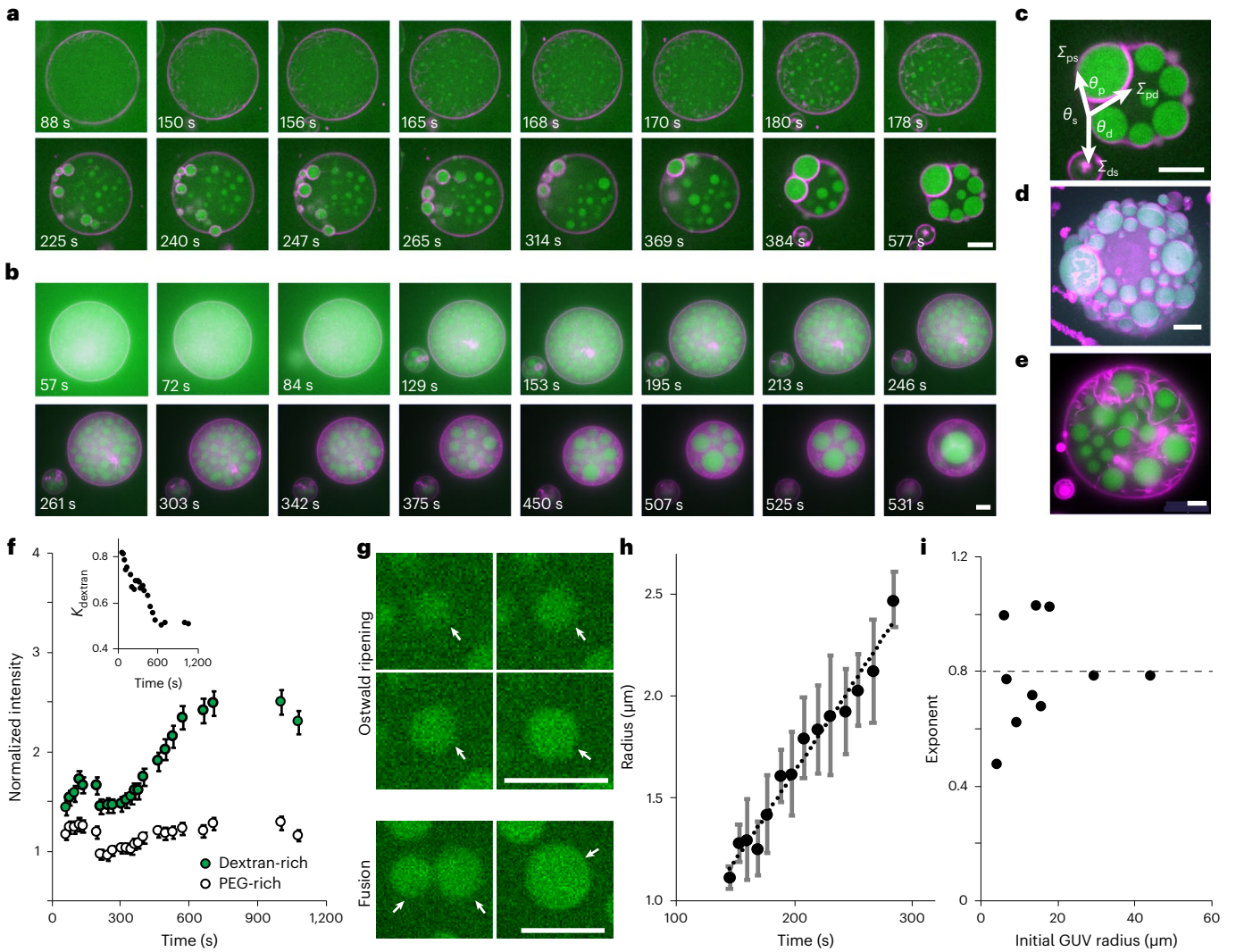

Fig. 2 | Phase transition trajectory inside giant vesicles. a,**b**, Selected frames from time-lapse videos of confocal fluorescence microscopy images (Supplementary Video 1) (**a**) and wide-field microscopy images (Supplementary Video 2) (**b**) of GUVs encapsulating a mixture of 6.0% (wt/wt) PEG 8 kDa and 6.4% (wt/wt) dextran 10 kDa doped with 0.001% AlexaFluor 488-dextran following immersion in 143 mM sucrose solution. **c**, Droplet shape characterization in terms of the three contact angles θ_p (74°), θ_d (121°) and θ_s (165°) corresponding to PEG-rich phase, dextran-rich phase and the exterior solution. Σ_{ps}, Σ_{pd} and Σ_{ds} represent tensions corresponding to the three interfaces (PEG-rich phase (p), dextran-rich phase (d) and the surrounding solution (s)). **d**, 3D image of GUVs encapsulating phase-separated droplets. **e**, Membrane tubule formation during LLPS. **f**, Changes in the fluorescence intensity of the labelled dextran during LLPS and (inset) the partition coefficient (K) of dextran in PEG-rich and dextran-rich phases. Data are presented as mean values ± 5% error ($n = 3$). For the number of dextran-rich droplets measured, see the source data. **g**, Examples of coarsening via Ostwald ripening and coalescence. Arrows indicate the coarsening droplets. **h**, Growth rate of a dextran-rich droplet for a single GUV ($n = 10$). The droplet growth follows $r = 0.007t^{\alpha}$, $\alpha = 1.02$, $R^2 = 0.96$. Data are presented as mean values ± s.d. ($n = 10$). For the number of dextran-rich droplets measured, see the source data. **i**, Exponent (α) as a function of the initial radius of the GUVs ($n = 10$). Each data point refers to an individual GUV. All GUVs imaged consist of a mixture containing 96.8% POPC, 2.2% DOPE-mPEG and 1% Rho-DOPE. Scale bar, 10 μm.

membrane boundary unbuds, restoring the initial spherical shape (Supplementary Video 3 and Extended Data Fig. 7). This ability of the membrane buds to robustly sequester their content (that is, dextran) as a distinct phase and subsequently redeliver, such as by an osmotically induced phase transition, appears curious (Supplementary Fig. 5). The former suggests a potential physical mechanism by which buds might select their molecular cargoes, such as in the formation of transport vesicles[61], while the latter appears phenomenologically similar to the fusion of vesicles carrying different cargos[62].

Systematic mapping of the phase-separation trajectory for a range of different weight fractions of PEG and dextran at a fixed total polymer concentration reveals that the essential dynamics described here remain largely unchanged (Fig. 3a–d, Extended Data Fig. 8 and Supplementary Videos 4–8). At low dextran concentrations, droplet sizes (and correspondingly the buds) are proportionately smaller; conversely, elevated dextran concentrations yield larger droplets and buds. In the limiting cases, the smallest membrane-bound buds produced at the lowest dextran concentrations merely decorate the membrane without budding (Fig. 3b, Extended Data Fig. 8a,b and Supplementary Videos 4 and 5), whereas at the highest dextran concentration tested, the reversal of the majority and droplet phases occurs. Under this condition, PEG-rich droplets wet the membrane, producing giant buds encapsulating the minority PEG phase (Fig. 3c, Extended Data Fig. 8d and Supplementary Video 7), consistent with the foregoing inference that the energetic cost of wetting the membrane by the droplet, that is, the complete-to-partial wetting transition[31,36], is smaller than the gain derived by the lowering of the interfacial area between the two aqueous phases.

https://doi.org/10.1038/s41557-023-01267-1

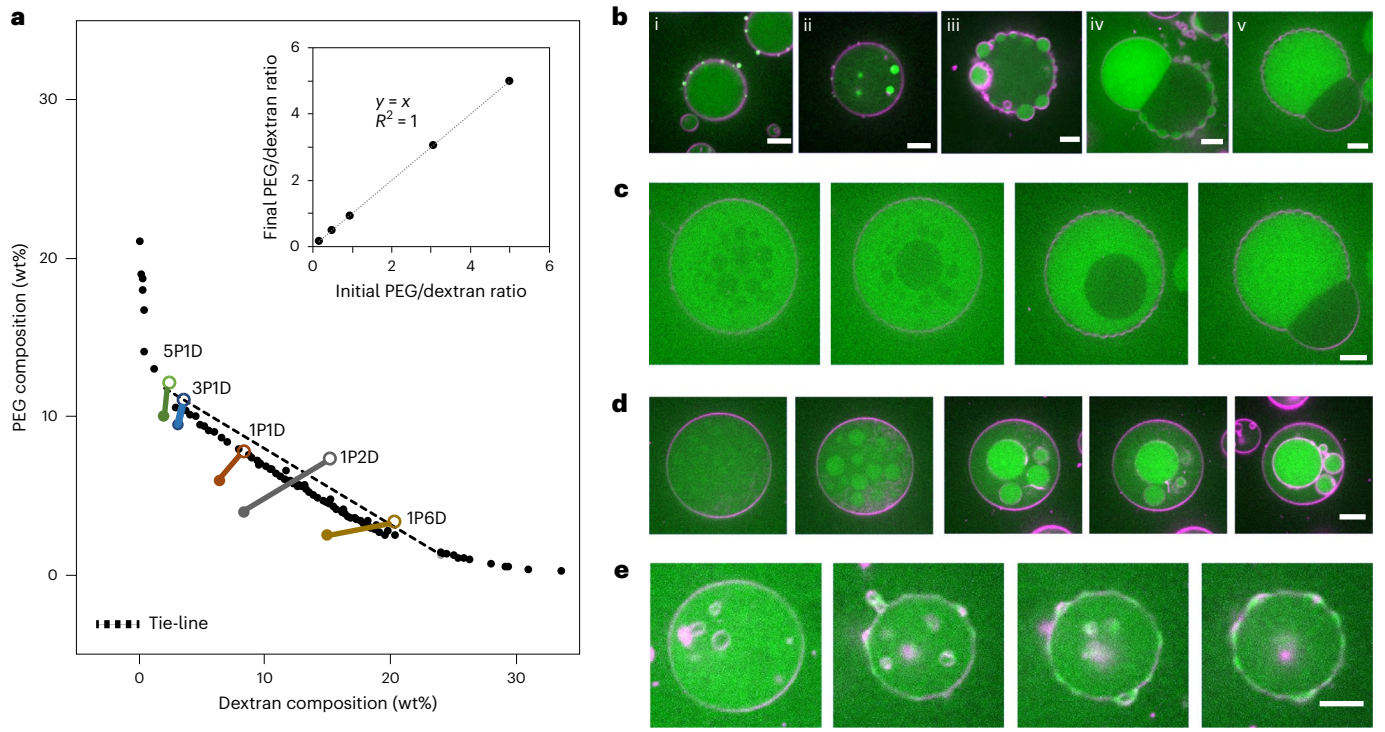

Fig. 3 | Composition dependence of polymer phase separation inside giant vesicles. a, Phase diagram for PEG 8 kDa and dextran 10 kDa in bulk solution. Binodal obtained by the cloud-point titration method in bulk solution. The data points (black) represent the concentrations that correspond to the disappearance of turbidity. The tie-line (black dashed line, from Fig. 1b), serves as a visual guide. The filled and open circles denote the initial, empirical PEG/Dex concentrations and final, theoretical PEG/Dex concentrations, respectively. The coloured, solid lines depict the transition from the one-phase region to the two-phase region. **b**, Representative confocal fluorescence microscopy image of GUVs encapsulating mixtures of (i) 5:1 (5P1D, Supplementary Video 4), (ii) 3:1 (3P1D, Supplementary Video 5), (iii) 1:1 (1P1D), (iv) 1:2 (1P2D, Supplementary Video 6) and (v) 1:6 (1P6D, Supplementary Video 7) ratios of PEG 8 kDa and dextran 10 kDa doped with 0.001% AlexaFluor 488-dextran upon immersion in (i) 143, (ii) 120, (iii) 143, (iv) 263 and (v) 298 mM sucrose solutions. All GUVs imaged consist of a mixture containing 96.8% POPC doped with 2.2% DOPE-mPEG and 1% Rho-DOPE. **c**, Time-lapse confocal fluorescence microscopy images of a single GUV encapsulating a mixture of a 1:6 (namely 1P6D, Supplementary Video 7) ratio of PEG 8 kDa and dextran 10 kDa, which represents PEG droplets assembling in the GUV and moving to the membrane surface as PEG-rich droplets. **d**, Confocal fluorescence microscopy image of GUVs consisting of a mixture containing 96.8% POPC, 2.2% DOPE-mPEG, 1% Rho-DOPE with 4.5% PEG 8 kDa and 2.02% dextran 450 kDa subjected to a 54 mM sucrose solution (Supplementary Video 8). **e**, Confocal fluorescence microscopy image of a single GUV consisting of a mixture containing 95% POPC, 4% GM1, 1% Rho-DOPE with 6.0% PEG 8 kDa and 6.4% dextran 10 kDa subjected to 143 mM sucrose solution (Supplementary Video 9). Scale bar, 10 μm.

In all of the experiments presented here, the membrane composition contained a finite proportion of PEG-derivatized lipid (DOPE-mPEG, 2.2 mol%), which was incorporated to facilitate GUV formation. These PEG-displaying dopants, however, may also act to preferentially wet the membrane by the incipient PEG-rich phase (allowing the dextran-rich phase to nucleate, grow and coarsen within the vesicular interior) during phase separation. Furthermore, to explore the effect of reversing the membrane preference for the wetting phase, we replaced DOPE-mPEG by the glycolipid GM1, which interacts preferentially with the dextran-rich phase (Methods). Remarkably, we found a complete and drastic reversal in the growth pattern (Fig. 3e and Supplementary Video 9): the dextran droplets almost exclusively nucleate, grow and coarsen at the membrane surface, suggesting a shift from homogeneous to heterogeneous nucleation, likely by spatially localizing the compositional fluctuations needed for phase separation in the vicinity of the membrane boundary.

The cumulated weight of the results presented here reveals the complex and dynamic interplay between the membrane boundary and the LLPS inside giant vesicles, altering equilibration pathways and stabilizing kinetically formed morphologies.

This dynamic relationship between phase separation in the aqueous bulk and the interfacial wetting-induced budding at the membrane surface raises an interesting question: how do the membrane's compositional degrees of freedom influence this interplay? In the cellular context, this simple question has important parallels: how do living cells control the sizes, shapes, distributions and other physical properties of the droplet condensates? What roles do membranes play in regulating LLPS inside the cell? How is the LLPS activity communicated to the membrane interface, where many signalling events occur? Recent studies highlight several biophysical pathways, such as the roles membranes play in (1) reducing concentration thresholds for LLPS by elevating local protein concentrations[20,22,63] and (2) facilitating nucleation and growth of membrane-bound protein condensates such as seen most prominently in T-cell signalling, where activation of T-cell receptors at the membrane surface triggers multi-phosphorylation of linker for activation of T cells, which in turn recruits additional proteins, Grb2 and divalent Son of Sevenless, producing rat sarcoma-activating[23] condensates at the membrane surface[64]. Yet, little is known about the relations between 2D lipid–lipid phase separation and membrane interactions of condensates produced by 3D LLPS.

To investigate whether the membrane association of dextran-rich liquid droplets can dynamically activate a membrane's compositional degrees of freedom, we replaced the single membrane lipids of our GUVs with a ternary mixture containing an equimolar concentration of POPC, cholesterol and sphingomyelin (2:2:1). To induce droplet formation in real time, we encapsulated an aqueous mixture containing 6 wt% PEG (8 kDa) and 6.4 wt% dextran (10 kDa) inside the GUVs and subjected them to hypertonic stress from a bath containing 143 mM

https://doi.org/10.1038/s41557-023-01267-1

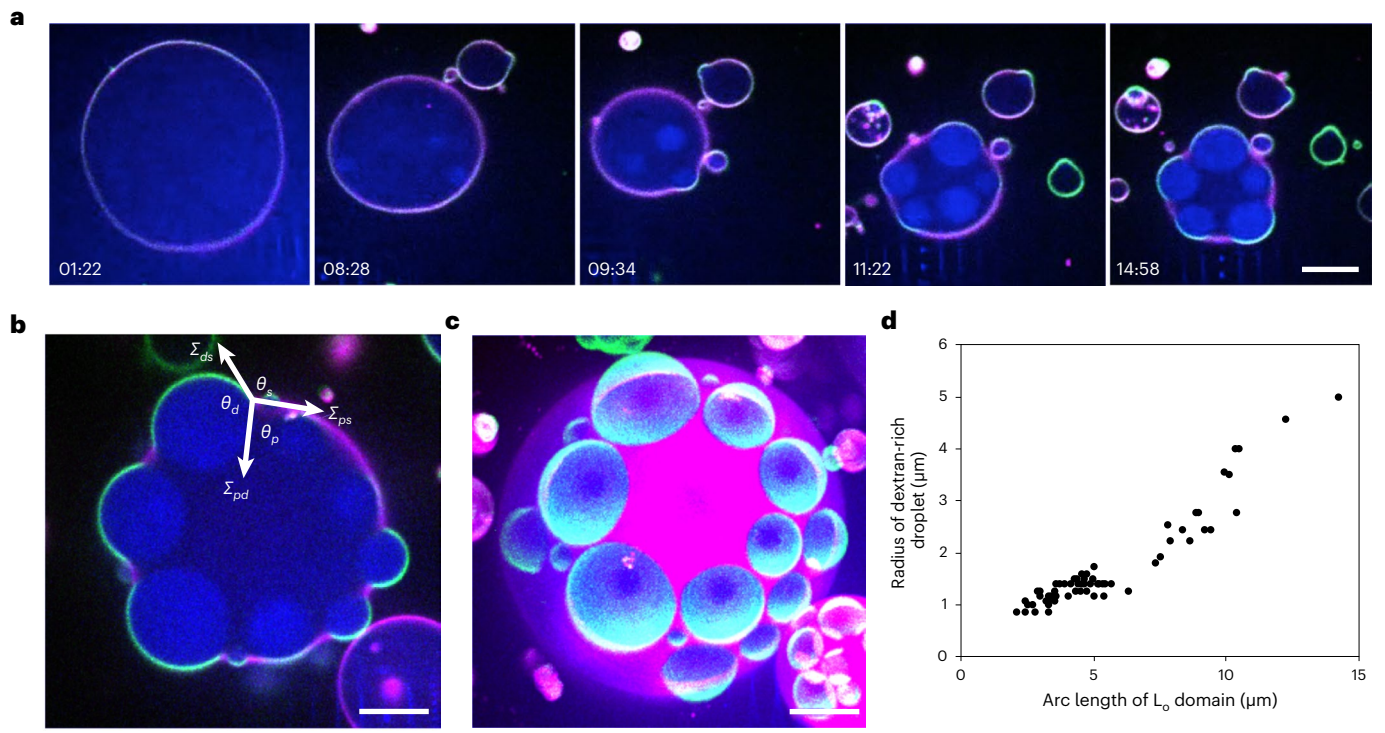

Fig. 4 | Coupling of bulk LLPS inside giant vesicles with membrane phase separation at the vesicle boundaries. a–**c**, Selected frames (**a**) and 2D (**b**) and 3D (**c**) images from a time-lapse video (Supplementary Video 10) of confocal fluorescence microscopy images of GUVs encapsulating a mixture of 6.0% (wt/wt) PEG 8 kDa and 6.4% (wt/wt) dextran 10 kDa doped with 0.001% AlexaFluor 647-Dextran upon immersion in 157 mM sucrose solution. The three contact angles θ_p (87°), θ_d (141°) and θ_s (132°) correspond to the PEG-rich phase, dextran-rich phase and exterior solution. Σ_{ps}, Σ_{pd} and Σ_{ds} represent three tensions along the three contact lines. The GUVs imaged consist of a mixture containing POPC:egg-SM:cholesterol in a ratio of 2:2:1, doped with 2.2% DOPE-mPEG, 1% Rho-DOPE and 3% NBD-PE. Scale bar, 10 μm. **d**, Plot of droplet size (diameter estimated from the arc delineating the bud) as a function of the arc length of the L_o domain ($n = 6$, where n refers to the number of GUVs), yielding a Pearson's R of 0.94.

sucrose. Time-lapse fluorescence microscopy images confirmed the general phase-ordering trajectory described earlier (Fig. 4a, Extended Data Fig. 9 and Supplementary Videos 10 and 11). Additionally, they reveal a remarkable redistribution of membrane components: upon droplet-induced membrane budding, the initial uniform distribution of the two phase-sensitive dyes in the membranes of the GUVs, reflecting a single homogeneous phase, is abandoned, replaced by a pattern of membrane fluorescence, fully commensurate with the pattern of droplet-induced buds: each bud is capped by the liquid-ordered (L_o) lipid phase enriched in cholesterol and sphingomyelin, and the skirt region between the buds is occupied by the complementary, phospholipid-rich liquid-disordered (L_d) phase (Fig. 4b,c). Comparing the arc length of the buds with the radii of the dextran-rich droplets (Fig. 4d) for 32 domains in six independent experiments, we find a strong positive correlation (Pearson's R, 0.94), further consistent with the notion that the domain sizes are controlled by droplet sizes.

There are several salient features of this emergent lipid phase pattern that match the underling droplet pattern, all of which can be readily understood in terms of well-known principles of membrane mechanics, dynamics and thermodynamics. First, perhaps the most remarkable aspect of our observations is the appearance of coexisting phases in direct correspondence with the emergence of droplet-induced membrane budding. Similar isothermal phase transitions have been observed previously in the absence of specific lipid–lipid or lipid–protein interactions, when multi-component lipid bilayers are subject to gradients of curvatures (such as occurs when tubes are pulled from giant vesicles[65]), under tension[66] (such as produced by osmotic stresses[66,67]) or fluctuations (such as modulated by adhesion[68]). In all of these cases, the plunge into phase coexistence occurs when membrane compositions are near the miscibility phase transition[65,69]. Moreover, the sizes of domains in equilibrated lipid bilayers are controlled by a balance of competition between line tension, which tends to increase domain sizes, and entropy, curvature and electrostatic repulsions, which oppose domain merger and promote subdivision[70,71]. In the present case, droplet wetting of the membrane introduces a consequential physical perturbation: it locally renders the membrane tense, suppresses thermal undulations, and produces curvature gradients in the neck region, separating the bud from the mother vesicle. Together, these mechanical-chemical factors control the observed lateral phase separation of lipids induced by the droplet-mediated budding.

Second, it is notable that the phase-separated domains are spatially commensurate with the underlying spatial patterns of membrane morphology and intravesicular polymer-enriched droplets. The lateral sorting of domains—albeit existing ones—in spatially defined curvature niches within single membranes has been observed in many independent contexts and over many different length scales[72]. A separate mechanism for similar domain alignment involves the preferential spatial localization of specific molecules, which are differentially solubilized between the two coexisting phases[73,74]. Indeed, a previous study by one of us[74] found that preferential interaction of a molecule (a PEG-terminated saturated lipid) solubilized preferentially in the L_o phase with the PEG-rich phase in the vesicular interior was sufficient to induce spatial ordering of pre-existing membrane domains in registry with the intravesicular bulk. In this same vein, the small concentration of L_d-phase partitioning DOPE-mPEG in the present study can readily explain the spatial positioning of the incipient membrane phases. Together, these considerations may explain our observations of simultaneous lipid phase separation and spatial localization of membrane domains driving an exquisite coupling of 3D LLPS within

the vesicular interior with the lateral phase separation of lipids at the membrane boundary.

Collectively, the results presented here exemplify the temporal morphological evolution during the segregative phase-ordering of a mixture of polymers inside giant vesicles following an abrupt quench. Our results could shed light on non-equilibrium behaviours of LLPS in cell-like compartments. The crowded nature of the cytoplasm, physical confinement in small volumes, and interactions with the proximal membrane, which is at once flexible, deformable and heterogeneous, can all be expected to influence the phase transition trajectories of induced LLPS. It can dynamically arrest phase separation, produce metastable spatial organization of coexisting phases, and couple the LLPS in the 3D interior with the 2D lipid–lipid phase separation at the membrane boundary—potentially suggesting a general physical–chemical principle that can drive mesoscale functional organization of membraneless organelles in living and artificial cells.

Online content

Any methods, additional references, Nature Portfolio reporting summaries, source data, extended data, supplementary information, acknowledgements, peer review information; details of author contributions and competing interests; and statements of data and code availability are available at https://doi.org/10.1038/s41557-023-01267-1.

References

1. Bray, A. J. Theory of phase-ordering kinetics. *Adv. Phys.* **43**, 357–459 (1994).
2. Binder, K. Collective diffusion, nucleation and spinodal decomposition in polymer mixtures. *J. Chem. Phys.* **79**, 6387–6409 (1983).
3. Onuki, A. *Phase Transition Dynamics* (Cambridge Univ. Press, 2002).
4. Binder, K. Spinodal decomposition in confined geometry. *J. Non-Equilib. Thermodyn.* **23**, 1–44 (1998).
5. Tanaka, H. Interplay between wetting and phase separation in binary fluid mixtures: roles of hydrodynamics. *J. Phys. Condens. Matter* **13**, 4637–4674 (2001).
6. Puri, S. J. Surface-directed spinodal decomposition. *J. Phys. Condens. Matter* **17**, R101–R142 (2005).
7. Jones, R. A. L., Norton, L. J., Kramer, E. J., Bates, F. S. & Wiltzius, P. Surface-directed spinodal decomposition. *Phys. Rev. Lett.* **66**, 1326–1329 (1991).
8. Wiltzius, P. & Cumming, A. Domain growth and wetting in polymer mixtures. *Phys. Rev. Lett.* **66**, 3000–3003 (1991).
9. Troian, S. M. Coalescence induced domain growth near a wall during spinodal decomposition. *Phys. Rev. Lett.* **71**, 1399–1402 (1993).
10. Tanaka, H. Double-phase separation in a confined, symmetrical binary mixture—interface quench effect unique to bicontinuous phase-separation. *Phys. Rev. Lett.* **72**, 3690–3693 (1994).
11. Berry, J., Brangwynne, C. P. & Haataja, M. Physical principles of intracellular organization via active and passive phase transitions. *Rep. Prog. Phys.* **81**, 046601 (2018).
12. Deshpande, S. & Dekker, C. Studying phase separation in confinement. *Curr. Opin. Colloid Interface* **52**, 101419 (2021).
13. Bagatolli, L. A. & Stock, R. P. Lipids, membranes, colloids and cells: a long view. *Biochim. Biophys. Acta Biomembr.* **1863**, 183684 (2021).
14. Last, M. G. F., Deshpande, S. & Dekker, C. pH-controlled coacervate-membrane interactions within liposomes. *ACS Nano* **14**, 4487–4498 (2020).
15. Agudo-Canalejo, J. et al. Wetting regulates autophagy of phase-separated compartments and the cytosol. *Nature* **591**, 142–146 (2021).
16. Yuan, F. et al. Membrane bending by protein phase separation. *Proc. Natl Acad. Sci. USA* **118**, e2017435118 (2021).
17. Babl, L., Merino-Salomon, A., Kanwa, N. & Schwille, P. Membrane mediated phase separation of the bacterial nucleoid occlusion protein Noc. *Sci. Rep.* **12**, 17949 (2022).
18. Alberti, S. Phase separation in biology. *Curr. Biol.* **27**, R1097–R1102 (2017).
19. Banani, S. F., Lee, H. O., Hyman, A. A. & Rosen, M. K. Biomolecular condensates: organizers of cellular biochemistry. *Nat. Rev. Mol. Cell Biol.* **18**, 285–298 (2017).
20. Li, P. L. et al. Phase transitions in the assembly of multivalent signalling proteins. *Nature* **483**, 336–340 (2012).
21. Shin, Y. & Brangwynne, C. P. Liquid phase condensation in cell physiology and disease. *Science* **357**, eaaf4382 (2017).
22. Banjade, S. & Rosen, M. K. Phase transitions of multivalent proteins can promote clustering of membrane receptors. *eLife* **3**, e04123 (2014).
23. Huang, W. Y. C. et al. A molecular assembly phase transition and kinetic proofreading modulate Ras activation by SOS. *Science* **363**, 1098–1103 (2019).
24. Andre, A. A. M. & Spruijt, E. Liquid–liquid phase separation in crowded environments. *Int. J. Mol. Sci.* **21**, 5908 (2020).
25. Crowe, C. D. & Keating, C. D. Liquid–liquid phase separation in artificial cells. *Interface Focus* **8**, 20180032 (2018).
26. Albertsson, P.-Å. in *Advances in Protein Chemistry* (eds Edsall, J. T., Anfinsen, C. B. & Richards, F. M.) Vol. 24, 309–341 (Academic Press, 1970).
27. Walde, P., Cosentino, K., Engel, H. & Stano, P. Giant vesicles: preparations and applications. *ChemBioChem* **11**, 848–865 (2010).
28. Deamer, D. W. & Bramhall, J. Permeability of lipid bilayers to water and ionic solutes. *Chem. Phys. Lipids* **40**, 167–188 (1986).
29. Helfrich, M. R., Mangeney-Slavin, L. K., Long, M. S., Djoko, Y. & Keating, C. D. Aqueous phase separation in giant vesicles. *J. Am. Chem. Soc.* **124**, 13374–13375 (2002).
30. Keating, C. D. Aqueous phase separation as a possible route to compartmentalization of biological molecules. *Acc. Chem. Res.* **45**, 2114–2124 (2012).
31. Li, Y. H., Lipowsky, R. & Dimova, R. Transition from complete to partial wetting within membrane compartments. *J. Am. Chem. Soc.* **130**, 12252–12253 (2008).
32. Li, Y. H., Lipowsky, R. & Dimova, R. Membrane nanotubes induced by aqueous phase separation and stabilized by spontaneous curvature. *Proc. Natl Acad. Sci. USA* **108**, 4731–4736 (2011).
33. Liu, Y. G., Lipowsky, R. & Dimova, R. Giant vesicles encapsulating aqueous two-phase systems: from phase diagrams to membrane shape transformations. *Front. Chem.* https://doi.org/10.3389/fchem.2019.00213 (2019).
34. Long, M. S., Jones, C. D., Helfrich, M. R., Mangeney-Slavin, L. K. & Keating, C. D. Dynamic microcompartmentation in synthetic cells. *Proc. Natl Acad. Sci. USA* **102**, 5920–5925 (2005).
35. Andes-Koback, M. & Keating, C. D. Complete budding and asymmetric division of primitive model cells to produce daughter vesicles with different interior and membrane compositions. *J. Am. Chem. Soc.* **133**, 9545–9555 (2011).
36. Kusumaatmaja, H., Li, Y., Dimova, R. & Lipowsky, R. Intrinsic contact angle of aqueous phases at membranes and vesicles. *Phys. Rev. Lett.* **103**, 238103 (2009).
37. Dimova, R. & Lipowsky, R. Giant vesicles exposed to aqueous two-phase systems: membrane wetting, budding processes and spontaneous tubulation. *Adv. Mater. Interfaces* **4**, 1600451 (2017).
38. Morales-Penningston, N. F. et al. GUV preparation and imaging: minimizing artifacts. *Biochim. Biophys. Acta Biomembr.* **1798**, 1324–1332 (2010).

39. Veatch, S. L. & Keller, S. L. Miscibility phase diagrams of giant vesicles containing sphingomyelin. *Phys. Rev. Lett.* **94**, 148101 (2005).
40. Dominak, L. M. & Keating, C. D. Polymer encapsulation within giant lipid vesicles. *Langmuir* **23**, 7148–7154 (2007).
41. Baumgart, T., Hunt, G., Farkas, E. R., Webb, W. W. & Feigenson, G. W. Fluorescence probe partitioning between L_o/L_d phases in lipid membranes. *Biochim. Biophys. Acta Biomembr.* **1768**, 2182–2194 (2007).
42. Hatti-Kaul, R. *Aqueous Two-Phase Systems: Methods and Protocols* (Humana Press, 2000).
43. Seifert, U. Configurations of fluid membranes and vesicles. *Adv. Phys.* **46**, 13–137 (1997).
44. Liu, Y. G., Agudo-Canalejo, J., Grafmuller, A., Dimova, R. & Lipowsky, R. Patterns of flexible nanotubes formed by liquid-ordered and liquid-disordered membranes. *ACS Nano* **10**, 463–474 (2016).
45. Lu, P. J. et al. Gelation of particles with short-range attraction. *Nature* **453**, 499–503 (2008).
46. Stradner, A. et al. Equilibrium cluster formation in concentrated protein solutions and colloids. *Nature* **432**, 492–495 (2004).
47. Binder, K. & Stauffer, D. Theory for slowing down of relaxation and spinodal decomposition of binary-mixtures. *Phys. Rev. Lett.* **33**, 1006–1009 (1974).
48. Binder, K. & Stauffer, D. Statistical-theory of nucleation, condensation and coagulation. *Adv. Phys.* **25**, 343–396 (1976).
49. Furukawa, H. A dynamic scaling assumption for phase-separation. *Adv. Phys.* **34**, 703–750 (1985).
50. Lifshitz, I. M. & Slyozov, V. V. The kinetics of precipitation from supersaturated solid solutions. *J. Phys. Chem. Solids* **19**, 35–50 (1961).
51. Voorhees, P. W. Ostwald ripening of 2-phase mixtures. *Annu. Rev. Mater. Sci.* **22**, 197–215 (1992).
52. Keblinski, P., Ma, W. J., Maritan, A., Koplik, J. & Banavar, J. R. Domain growth near a wall in spinodal decomposition. *Phys. Rev. Lett.* **72**, 3738 (1994).
53. Baumgart, T., Hess, S. T. & Webb, W. W. Imaging coexisting fluid domains in biomembrane models coupling curvature and line tension. *Nature* **425**, 821–824 (2003).
54. Julicher, F. & Lipowsky, R. Domain-induced budding of vesicles. *Phys. Rev. Lett.* **70**, 2964–2967 (1993).
55. Cakmak, F. P. & Keating, C. D. Combining catalytic microparticles with droplets formed by phase coexistence: adsorption and activity of natural clays at the aqueous/aqueous interface. *Sci. Rep.* **7**, 3215 (2017).
56. Semrau, S., Idema, T., Schmidt, T. & Storm, C. Membrane-mediated interactions measured using membrane domains. *Biophys. J.* **96**, 4906–4915 (2009).
57. Ursell, T. S., Klug, W. S. & Phillips, R. Morphology and interaction between lipid domains. *Proc. Natl Acad. Sci. USA* **106**, 13301–13306 (2009).
58. Yanagisawa, M., Imai, M., Masui, T., Komura, S. & Ohta, T. Growth dynamics of domains in ternary fluid vesicles. *Biophys. J.* **92**, 115–125 (2007).
59. Laradji, M. & Sunil Kumar, P. B. Dynamics of domain growth in self-assembled fluid vesicles. *Phys. Rev. Lett.* **93**, 198105 (2004).
60. Laradji, M. & Kumar, P. B. Anomalously slow domain growth in fluid membranes with asymmetric transbilayer lipid distribution. *Phys. Rev. E* **73**, 040901 (2006).
61. Kuehn, M. J., Herrmann, J. M. & Schekman, R. COPII-cargo interactions direct protein sorting into ER-derived transport vesicles. *Nature* **391**, 187–190 (1998).
62. Bonifacino, J. S. & Glick, B. S. The mechanisms of vesicle budding and fusion. *Cell* **116**, 153–166 (2004).
63. Case, L. B., Ditlev, J. A. & Rosen, M. K. Regulation of transmembrane signaling by phase separation. *Annu. Rev. Biophys* **48**, 465–494 (2019).
64. Su, X. L. et al. Phase separation of signaling molecules promotes T cell receptor signal transduction. *Science* **352**, 595–599 (2016).
65. Roux, A. et al. Role of curvature and phase transition in lipid sorting and fission of membrane tubules. *EMBO J.* **24**, 1537–1545 (2005).
66. Oglecka, K., Rangamani, P., Liedberg, B., Kraut, R. S. & Parikh, A. N. Oscillatory phase separation in giant lipid vesicles induced by transmembrane osmotic differentials. *eLife* **3**, e03695 (2014).
67. Hamada, T., Kishimoto, Y., Nagasaki, T. & Takagi, M. Lateral phase separation in tense membranes. *Soft Matter* **7**, 9061–9068 (2011).
68. Gordon, V. D., Deserno, M., Andrew, C. M. J., Egelhaaf, S. U. & Poon, W. C. K. Adhesion promotes phase separation in mixed-lipid membranes. *Europhys. Lett.* **84**, 48003 (2008).
69. Tian, A. & Baumgart, T. Sorting of lipids and proteins in membrane curvature gradients. *Biophys. J.* **96**, 2676–2688 (2009).
70. Kuzmin, P. I., Akimov, S. A., Chizmadzhev, Y. A., Zimmerberg, J. & Cohen, F. S. Line tension and interaction energies of membrane rafts calculated from lipid splay and tilt. *Biophys. J.* **88**, 1120–1133 (2005).
71. Seul, M. & Andelman, D. Domain shapes and patterns—the phenomenology of modulated phases. *Science* **267**, 476–483 (1995).
72. Callan-Jones, A., Sorre, B. & Bassereau, P. Curvature-driven lipid sorting in biomembranes. *Cold Spring Harb. Perspect. Biol.* **3**, a004648 (2011).
73. Zhao, J., Wu, J. & Veatch, S. L. Adhesion stabilizes robust lipid heterogeneity in supercritical membranes at physiological temperature. *Biophys. J.* **104**, 825–834 (2013).
74. Cans, A. S., Andes-Koback, M. & Keating, C. D. Positioning lipid membrane domains in giant vesicles by micro-organization of aqueous cytoplasm mimic. *J. Am. Chem. Soc.* **130**, 7400–7406 (2008).

Methods

Materials

The POPC, egg sphingomyelin, cholesterol, DOPE-mPEG, GM1 ganglioside (brain, ovine-sodium salt) (GM1), Rho-DOPE and NBD-PE were acquired from Avanti Polar Lipids. Poly(butadiene-b-ethylene oxide) ($PBD_{22}PEO_{14}$), with average molecular weights of 1,200 g mol^{-1} and 600 g mol^{-1} for the PBD and PEO blocks, respectively, was purchased from Polymer Source. Glucose, PEG (8 kDa) (M_W 8,000 Da, batch no. BCCF6737), dextran from *Leuconostoc mesenteroides* (dextran (10 kDa), M_W 9,000–11,000 Da, lot no. BCCC7068) and dextran from *Leuconostoc* spp. (dextran (450 kDa), M_W 450,000–650,000 Da) were obtained from Sigma-Aldrich. AlexaFluor 488-dextran (M_W 10 kDa) and AlexaFluor 647-dextran (M_W 10 kDa) were purchased from ThermoFisher Scientific. Sucrose was obtained from EMD Chemicals. Chloroform was purchased from Fisher Scientific. Ninety-six-well glass-bottom plates were obtained from MatTek Corporation. Indium tin oxide (ITO)-coated glass slides (resistance 4–30 Ω) were obtained from Delta Technologies. All chemicals were used without further purification.

Preparation of GUVs

The GUVs were prepared by adapting a previously established electroformation technique[75]. We began with the preparation of three separate stock solutions (2 mg ml^{-1}) in chloroform: (1) a 2:2:1 mol ratio mixture of POPC, sphingomyelin and cholesterol containing 2.2 mol% DOPE-mPEG, 1 mol% Rho-DOPE and 3 mol% NBD-PE; (2) 96.8 mol% POPC doped with 2.2 mol% DOPE-mPEG and 1 mol% Rho-DOPE; (3) 96 mol% POPC doped with 4 mol% GM1 and 1 mol% Rho-DOPE . Small aliquots (~15 µl) of the stock solutions were spread on the conductive sides of each of the two ITO-coated slides, and dried under vacuum overnight. The dried film on one of the two slides was then directly hydrated either with 14 mM sucrose (control experiments) or with polymer solutions mixtures[33,37,40]. The latter included mixtures of (1) 6.0 wt% PEG (8 kDa) and 6.4 wt% dextran (10 kDa), (2) 4.5 wt% PEG (8 kDa) and 2.02 wt% dextran (10 kDa), (3) 9.5 wt% PEG (8 kDa) and 3.1 wt% dextran (10 kDa), (4) 10 wt% PEG (8 kDa) and 2 wt% dextran (10 kDa), (5) 4 wt% PEG (8 kDa) and 8.3 wt% dextran (10 kDa) and (6) 2.5 wt% PEG (8 kDa) and 15 wt% dextran (10 kDa). Specifically, to prepare 6.0 wt% PEG (8 kDa) and 6.4 wt% dextran (10 kDa) solution, we first prepared stock solution of 40 wt% (~50 mM) PEG (8 kDa) and 20 wt% (~20 mM) dextran (10 kDa), respectively. Subsequently, 0.6 g of the 40 wt% PEG (8 kDa) stock solution, 1.28 g of the 20 wt% dextran (10 kDa) stock solution and 2.12 g of deionized (DI) water were mixed thoroughly.

The solution droplet on the ITO slide was contained using a 1-mm-thick rubber 'O' ring (~20-mm diameter, Ace Hardware) and sealed with high-vacuum grease (Dow Corning). A water-tight chamber was then created by sealing the second ITO slide over the ring, ensuring that no visible air bubbles were trapped inside. Using a function generator, a 4-V_{pp} a.c. sine wave was then applied across the two slides at 10 Hz for 3 h, followed by a 4-V_{pp} a.c. square wave at 2 Hz for 2 h. During electroformation, the ITO sandwich was covered with an aluminium foil to protect from light. Upon electroformation, the ITO sandwich was disassembled and the solution containing GUVs was collected using a pipette. The GUVs were either used immediately or stored at 4 °C. All vesicles were used within a week of preparation.

Spinning disk confocal fluorescence microscopy

Spinning disk confocal fluorescence microscopy measurements were performed using an Intelligent Imaging Innovations Marianas Digital Microscopy Workstation (3i Denver) fitted with a CSU-X1 spinning disk head (Yokogawa Musashino-sh) and a Quantem512SC EMCCD camera (Photometrics Tuscon). Fluorescence micrographs were obtained using oil immersion objectives (Zeiss Fluor ×40 (NA 1.3), Zeiss Plan-Fluor ×63 (NA 1.4) and Zeiss Fluor ×100 (NA 1.46); Carl Zeiss). Wide-field fluorescence microscopy measurements were performed on a Carl Zeiss Axio Observer Z1 inverted microscope, fitted with Zeiss Plan-NeoFluar ×63 (NA 1.25). Samples of osmotically balanced GUVs were prepared as described in the previous section. In a typical experiment, the glass-bottom 96-well plate containing osmolyte-laden solution (195 µl) was mounted onto the microscope, and, once oiled, the objectives were raised to form a meniscus between the cover glass and the objective. To introduce osmotic gradients in real time, GUV suspension (5 µl) was added to the solution in the sample chambers. The focal plane was set close to the equatorial plane of the GUV where most of the droplets were in focus. The droplets close to the equatorial plane of the GUV were focused. Rho-DOPE (ex./em., 560/583) was exposed with a 50-mW 561 laser line. AlexaFluor 488-dextran (ex./em., 495/519), NBD-PE (ex./em., 460/535) were exposed with a 50-mW 488 laser line. AlexaFluor 647-dextran (ex./em., 650/668) was exposed with a 50-mW 651 laser line. The images are subsequently analysed using ImageJ (http://rsbweb.nih.gov/ij/), a public-domain software, and Slidebook digital microscopy imaging software (3i Denver). A circle delineating the droplet was drawn and the radius of the circle was calculated from its area.

Phase diagrams of the polymer mixtures in bulk solutions

The binodal lines determining the phase diagrams of the aqueous two-phase polymer mixtures were constructed using the standard cloud-point method[76]. Briefly, 40 wt% PEG (8 kDa) stock solution and 30 wt% dextran (10 kDa) stock solution were first prepared. A known mass of ~5 g 40 wt% PEG (8 kDa) was weighed and placed in a glass vial. Small aliquots of 30 wt% dextran (10 kDa) solution were added dropwise into the PEG (8 kDa) solution and mixed after each addition until the solutions became cloudy. This point was taken to indicate a passage across the binodal line into the two-phase region. Water was subsequently added to the mixture, also in a dropwise manner, and allowed to mix after each addition, until the mixture became clear and homogeneous. This point was taken to indicate the transition back across the binodal curve to the homogeneous phase. The process was repeated to collect several points along the binodal line.

Measurements of PEG and dextran concentrations via refractometry and polarimetry

The concentrations of dextran and PEG within distinct phases were determined using a combination of refractometry and polarimetry[77]. Bulk dextran/PEG ATPS were prepared in triplicate using the reported total weights. The dextran- and PEG-rich phases were physically separated via pipette, with the exception of the 6%/6.4% dextran/PEG system, which was single phase. Calibration standards were freshly prepared. The dextran concentration within each phase was measured first by polarimetry (model no. 343 Polarimeter, PerkinElmer). Dextran standards were used to establish a calibration curve relating the angle of rotation to dextran concentration. PEG is not optically active and therefore does not contribute to the measured angle. The refractive indices of individual phases were measured via refractometry (Abbe Auto Refractometer, Leica Geosystems). The optical contribution of dextran on the measured refractive index for each phase was calculated using the concentration measured via polarimetry and the refractometry dextran calibration curve. This value was subtracted from the total measured refractive index to determine the contribution attributed to PEG. The PEG concentration was then determined using the refractometer calibration curve. Each measurement was performed in triplicate on samples that were prepared in triplicate over multiple days of analysis. The results are summarized in Supplementary Table 1.

Osmotic pressure measurements

The osmotic pressure of each phase was determined using osmometry. The osmolality of the PEG- (8 kDa) and dextran- (10 kDa) rich phases were measured using a Wescor 5100C Vapor Pressure Deficit Osmometer (Wescor Inc.), calibrated with NaCl standard solutions (Wescor). The osmotic pressure, Π (MPa), of each solution was calculated from

osmolality measurements using the Van't Hoff equation: $\Pi = RTc$, where c is the osmolality (in mol kg^{-1}) and RT = 2.446 kg MPa mol^{-1} at 21 °C.

Data processing

Images were processed using ImageJ, a public-domain software obtained from http://rsbweb.nih.gov/ij/.

PEG-dextran aqueous two-phase system

The thermodynamic driving forces for the phase separation include synergistic contributions[78] from two distinct molecular mechanisms: (1) energetically unfavourable interactions between the segments of the two polymers overcoming the loss of mixing entropy[79] and (2) the repulsive force or an 'epistructural tension' arising from the differences in water structure surrounding the two polymers[80]. Because of the weak nature of these interactions, the effective interfacial tension between the two aqueous phases is low—three to four orders of magnitude lower than typical liquid–liquid systems[81]—and highly adjustable. Its magnitude ranges between 1 and 1,000 μN m^{-1} and depends sensitively on the proximity to the critical point and polymer properties, including concentrations, molecular weights and the disparities in their molecular weights[33,82]. Moreover, both PEG and dextran are also efficient crowding agents capable of minimally recapitulating macromolecular crowding, such as exists in cellular cytoplasm[83].

GM1-containing membranes

Previous studies established that GM1 can selectively desorb from the outer leaflets of bilayer lipid membranes, thereby producing membrane spontaneous curvature. For GUVs, such desorption can induce spontaneous tubulation and drive lipid phase separation producing GM1-enriched lipid domains[84]. Under the conditions used (4 mol% GM1, ~21 °C) in our studies, we find little or no evidence for such gross deformations.

Time-resolved measurements of the growth of phase-separated droplets

Note that these observation do not correspond to the nucleation or early growth events, which must occur almost instantaneously because osmotically mediated water efflux occurs rapidly (millisecond timescales). Rather, these observations reflect late-stage coarsening when the droplets have grown to optically resolved sizes.

Statistical validation of LLPS dynamics

Both the LLPS and budding events reported here are highly reproducible. Visualizing the behaviour of 55 GUVs in a single experiment, the phenomenology was robustly evident in 52 GUVs (~95%; Supplementary Table 2). Comparable statistics (>90%) were seen in more than a dozen (n = 14) independent experiments carried out under nominally identical conditions. The qualitative phenomenology was also reproducible for a variety of GUV sizes (Fig. 2i and Extended Data Fig. 5).

Comparing the behaviours of GUVs (n = 10) of varying initial sizes between 5 μm and 50 μm, the phenomena of osmotically mediated LLPS and budding were robustly evident. In all cases, the dextran droplets nucleated in the lumen of GUVs and displayed comparable coarsening (Fig. 2i and Extended Data Fig. 5). There was, however, a subtle, but noticeable, dependence on the size of the GUVs: smaller GUVs, in the vicinity of 10-μm diameter, displayed larger variations in the coarsening exponent, with the larger ones (>20 μm) converging to ~0.8 with a noticeably narrower distribution, potentially suggesting the growing importance of gravity in larger vesicles[85]. The limiting morphology in all cases was also the one characterized by droplets wetting and budding the membrane.

Membrane wetting by the droplets

The trafficking of dextran-rich droplets to the membrane surface raises a curious question: why does the dextran-enriched droplet phase wet the membrane, which contains PEG-preferential mPEG molecules? From the vantage point of the membrane, droplet wetting corresponds to a complete-to-partial wetting transition[31,36] in which the membrane surface, which was initially wetted by the majority PEG-rich phase exclusively, becomes wetted by both coexisting phases. This wetting transition can be understood in terms of the changing balance between three relevant interfacial interactions[31]—Σ_{pm}, Σ_{dm} and Σ_{pd}—which represent the interfacial tensions associated with the interfaces between the PEG-rich phase (p), the dextran-rich phase (d) and the membrane (m) (Fig. 2c). During the early stages (t < 200 s)—when the dextran-rich droplets are growing by accretion of dextran molecules and have yet to achieve equilibrium composition—the interfacial tension Σ_{pd} is still low, and the membrane remains wetted by the PEG-enriching phase ($\Sigma_{pd} < \Sigma_{dm} - \Sigma_{pm}$). Over time, as growth due to molecular exchanges enriches the droplets and depletes the bath in terms of dextran concentrations, σ_{pd} continues to rise and crosses ($t \approx 200$ s) a threshold ($\Sigma_{pd} \cong \Sigma_{dm} - \Sigma_{pm}$), beyond which the energetic cost of wetting the membrane by the dextran-rich droplet is smaller than the gain obtained by the lowering of the interfacial area between the two aqueous phases.

In all of the experiments reported in this Article, the membrane compositions contained a finite proportion of PEG-derivatized lipid (DOPE-mPEG, 2.2 mol%), which is incorporated to facilitate GUV formation. These PEG-displaying dopants, however, may also act to preferentially wet the membrane by the incipient PEG-rich phase (allowing the dextran-rich phase to nucleate, grow and coarsen within the vesicular interior) during phase separation. We confirmed this preferential wetting scenario through an independent experiment, which used quasi-single-component PEGylated GUVs. Specifically, we used 99 mol% polybutadiene$_{22}$-b-polyethyleoxide$_{14}$ ($PBD_{22}PEO_{14}$.) GUV doped with 1 mol% Rho-DOPE. Upon osmotic deflation, dextran-rich droplets nucleate, grow and coarsen exclusively within the lumen of the GUVs, away from the membrane surface, lending further support to the foregoing notion that the PEG dopants are preferentially wetted by the incipient PEG phase (Extended Data Fig. 10 and Supplementary Video 12).

Tubule formation

Previous studies have suggested that the spontaneous formation of membrane nanotubes upon osmotic deflation is driven by asymmetry[33,44,86]. Specifically, these studies suggest that the initial membrane deformation into a nascent bud is prompted by an in situ-generated negative spontaneous curvature because of the asymmetric adsorption of PEG polymer to the inner leaflet of the membrane surface[33]. They further suggest that these nascent spherical buds grow via a rapid flow of lipids producing a string of buds, which relax into cylindrical tubes[44].

Molecular weight dependence

The phase separation in the PEG-dextran ATPS system is known to depend on the molecular weights of the two phase-separating components. Polymers of higher molecular weight (1) depress the binodal to lower concentrations, thus favouring phase separation, (2) lengthen the tie-lines, segregating the polymers more effectively, and (3) increase the magnitude of interfacial tension[81]. These effects become more pronounced when the ratio of the molecular weight of the two polymers is also large[87]. To characterize how the better segregation of polymers and higher interfacial tension influence the kinetic interplay of droplet coarsening and budding, we repeated the experiments by substituting dextran 10 kDa by dextran 450 kDa. We find that the droplets coarsen to larger diameters, often producing single large droplets, before adhering to the membrane (Fig. 3d and Supplementary Video 8). This is not surprising, because elevated interfacial tension between the incipient coexisting phases increases the thermodynamic driving force for droplet coalescence, allowing rapid equilibration of the ATPS phases within the vesicular lumen before budding. Subsequently, single large droplets bud, producing morphologies similar to those typically

obtained by a slow and stepwise approach to phase separation under near-equilibrium conditions[37].

Data availability

Data supporting the findings of this study are available within this article and its supplementary information. Source data are provided with this paper.

References

75. Angelova, M. I. & Dimitrov, D. S. Liposome electroformation. *Faraday Disc. Chem. Soc.* **81**, 303–311 (1986).
76. Hatti-Kaul, R. *Aqueous Two-Phase Systems: Methods and Protocols* Vol. 11 (Humana Press, 2000).
77. Albertsson, P.-Å. & Tjerneld, F. in *Methods in Enzymology* Vol. 228, 3–13 (Academic Press, 1994).
78. Ribeiro, S. S., Samanta, N., Ebbinghaus, S. & Marco, J. C. The synergic effect of water and biomolecules in intracellular phase separation. *Nat. Rev. Chem.* **3**, 552–561 (2019).
79. Gustafsson, A., Wennerstrom, H. & Tjerneld, F. The nature of phase separation in aqueous two-polymer systems. *Polymer* **27**, 1768–1770 (1986).
80. Zaslavsky, B. Y. & Uversky, V. N. In aqua veritas: the indispensable yet mostly ignored role of water in phase separation and membrane-less organelles. *Biochemistry* **57**, 2437–2451 (2018).
81. Forciniti, D., Hall, C. K. & Kula, M. R. Interfacial tension of polyethyleneglycol-dextran-water systems: influence of temperature and polymer molecular weight. *J. Biotechnol.* **16**, 279–296 (1990).
82. Liu, Y. G., Lipowsky, R. & Dimova, R. Concentration dependence of the interfacial tension for aqueous two-phase polymer solutions of dextran and polyethylene glycol. *Langmuir* **28**, 3831–3839 (2012).
83. Zhou, H. X., Rivas, G. N. & Minton, A. P. Macromolecular crowding and confinement: biochemical, biophysical, and potential physiological consequences. *Annu. Rev. Biophys* **37**, 375–397 (2008).
84. Dasgupta, R., Miettinen, M. S., Fricke, N., Lipowsky, R. & Dimova, R. The glycolipid GM1 reshapes asymmetric biomembranes and giant vesicles by curvature generation. *Proc. Natl Acad. Sci. USA* **115**, 5756–5761 (2018).
85. Feric, M. & Brangwynne, C. P. A nuclear F-actin scaffold stabilizes ribonucleoprotein droplets against gravity in large cells. *Nat. Cell Biol.* **15**, 1253–1259 (2013).
86. Zhao, Z. L. et al. Super-resolution imaging of highly curved membrane structures in giant vesicles encapsulating molecular condensates. *Adv. Mater.* **34**, 2106633 (2022).
87. Forciniti, D., Hall, C. K. & Kula, M. R. Influence of polymer molecular weight and temperature on phase composition in aqueous two-phase systems. *Fluid Ph. Equilib.* **61**, 243–262 (1991).

Acknowledgements

We thank the MCB Light Microscopy Imaging Facility, which is a UC-Davis Campus Core Research Facility, for the use of their spinning disk confocal fluorescence microscope. The 3i Marianas spinning disk confocal used in this study was purchased using National Institutes of Health Shared Instrumentation grant 1S10RR024543-01. W.-C.S., D.L.G. and A.N.P. acknowledge funding from the National Science Foundation (DMR-1810540). J.C.S.H. and A.N.P. acknowledge funding and support from the Singapore Centre for Environmental Life Sciences Engineering and the Institute for Digital Molecular Analytics and Science, Nanyang Technological University. C.D.K. and A.T.R. were supported by the US Department of Energy, Office of Science, Basic Energy Sciences under award no. DE-SC0008633.

Author contributions

W.-C.S., C.D.K. and A.N.P. conceived and designed the study. W.-C.S., J.C.S.H. and D.L.G. designed and executed the experimental protocols for the preparation of the vesicle system and carried out the fluorescence microscopy measurements. A.T.R. performed the polarimetry and refractometry measurements of the phase compositions. W.-C.S., J.C.S.H., C.D.K. and A.N.P. co-wrote the paper, with contributions from all authors.

Competing interests

The authors declare no competing interests.

Additional information

Extended data is available for this paper at https://doi.org/10.1038/s41557-023-01267-1.

Supplementary information The online version contains supplementary material available at https://doi.org/10.1038/s41557-023-01267-1.

Correspondence and requests for materials should be addressed to Christine D. Keating or Atul N. Parikh.

Peer review information *Nature Chemistry* thanks Rumiana Dimova and the other, anonymous, reviewer(s) for their contribution to the peer review of this work.

https://doi.org/10.1038/s41557-023-01267-1

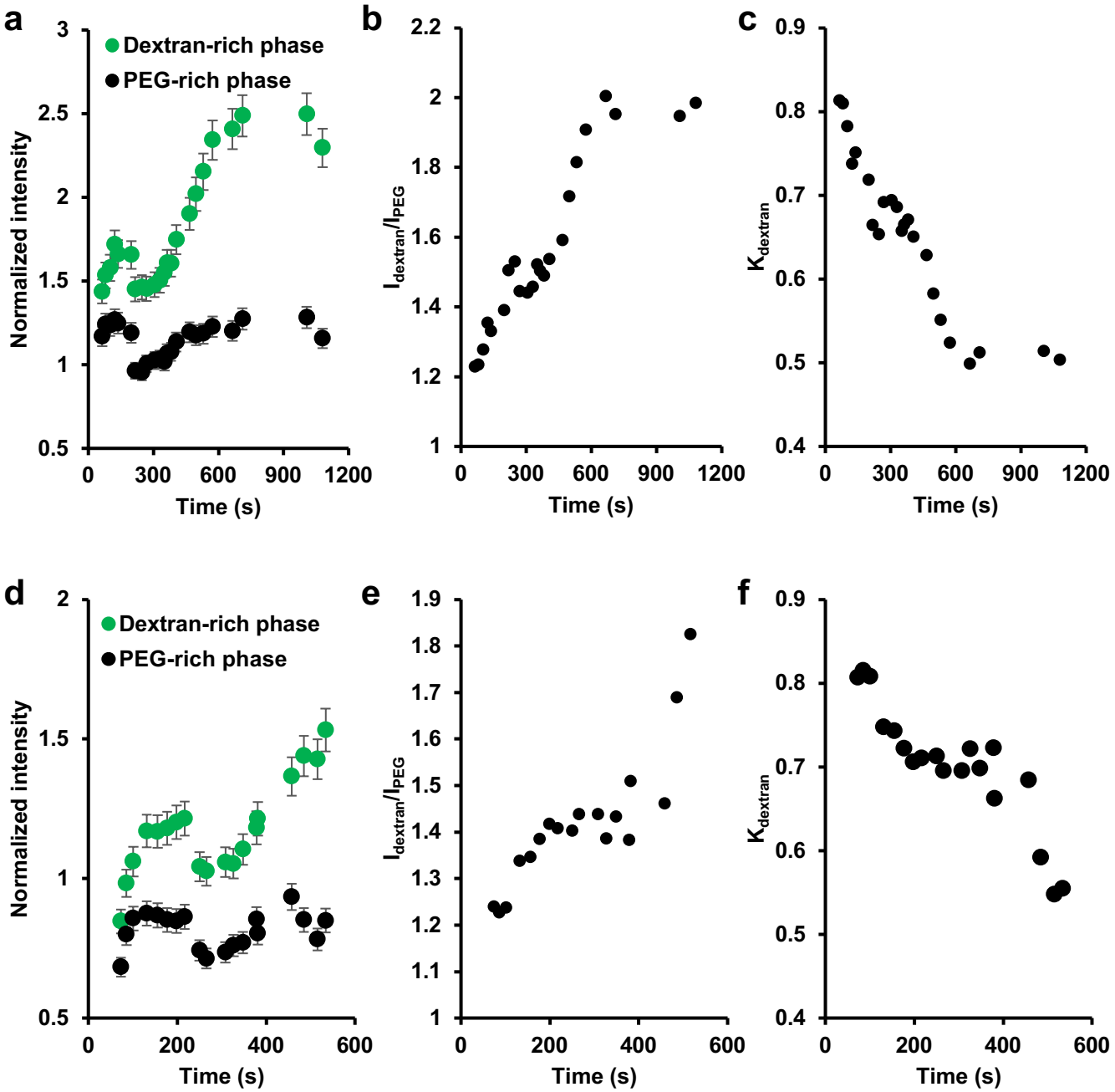

Extended Data Fig. 1 | Fluorescence intensity measurements of solution encapsulated in an LLPS GUV to determine the partition coefficient (K) of dextran in PEG-rich and dextran-rich phases. (a, d) Normalized fluorescent intensity profile of dextran (Alexa flour® 488 dextran) in PEG-rich and dextran-rich phases after phase separation. Photobleaching effect was taken into account in the calculation (Supplementary Fig. S2). Data are presented as mean values ± 5% error, (n = 3). For the number of dextran-rich droplets measured, refer to Supplementary Data. (b, e) The ratio of fluorescence intensity of dextran-rich phase versus the PEG-rich phase. (c, f) Measurement of partition coefficient (K) of dextran in LLPS GUV. GUVs contain 96.8 mol% POPC, 2.2 mol% DOPE-mPEG, and 1 mol% Rho-DOPE encapsulate a mixture of 6 wt% PEG 8 kDa and 6.4 wt% dextran 10 kDa upon immersion in 143 mM sucrose solution.

https://doi.org/10.1038/s41557-023-01267-1

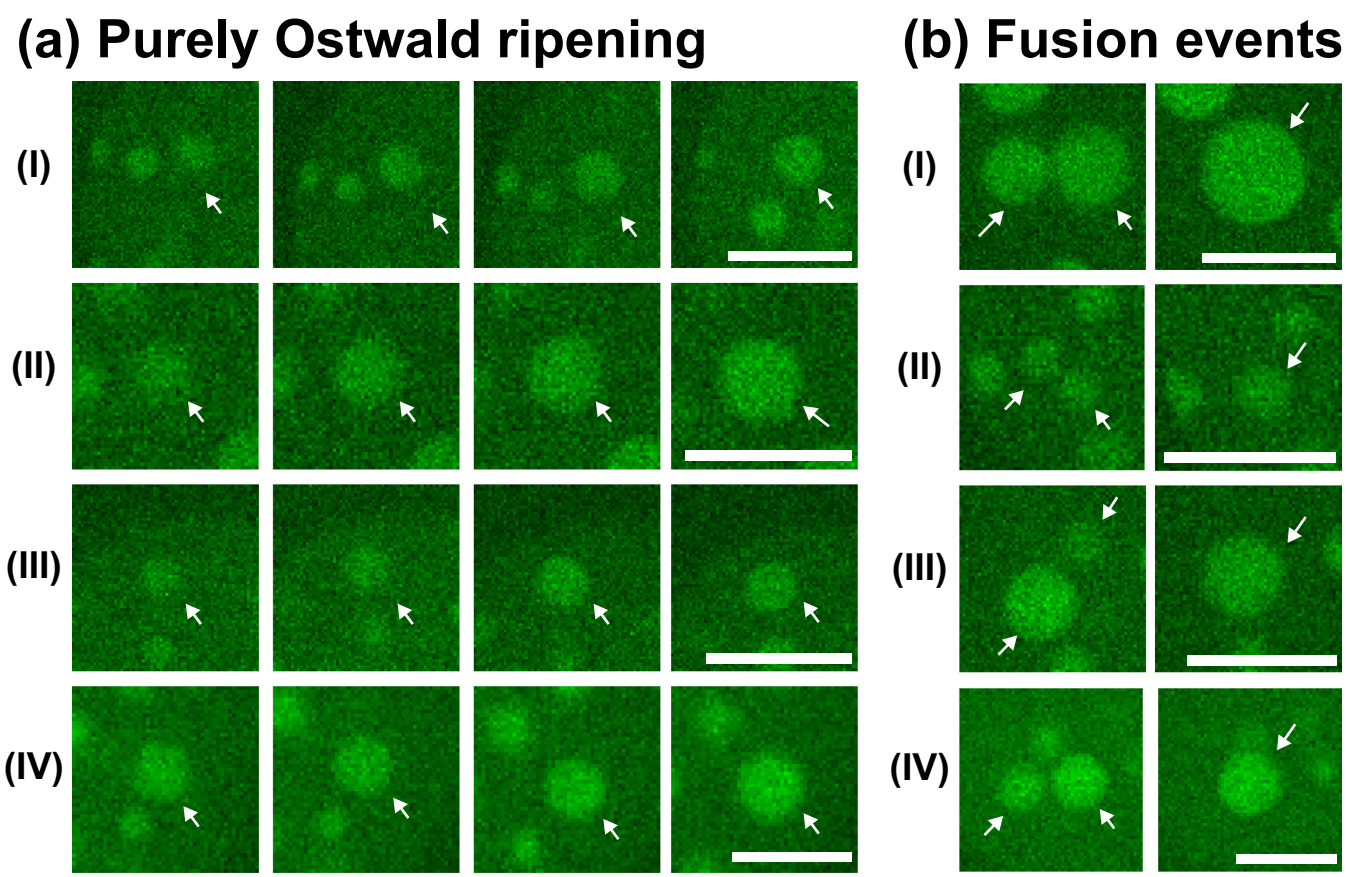

Extended Data Fig. 2 | Ostwald ripening and fusion trajectories. Trajectory of individual droplets during coarsening in GUVs encapsulating a mixture of 6.0% (w/w) PEG 8 kDa and 6.4% (w/w) dextran 10 kDa doped with 0.001% AlexaFluor® 488-Dextran upon immersion in 143 mM sucrose solution. (a) Purely Ostwald ripening. (b) Fusion events. Arrows indicate coarsening droplets. All scale bar, 10 µm.

https://doi.org/10.1038/s41557-023-01267-1

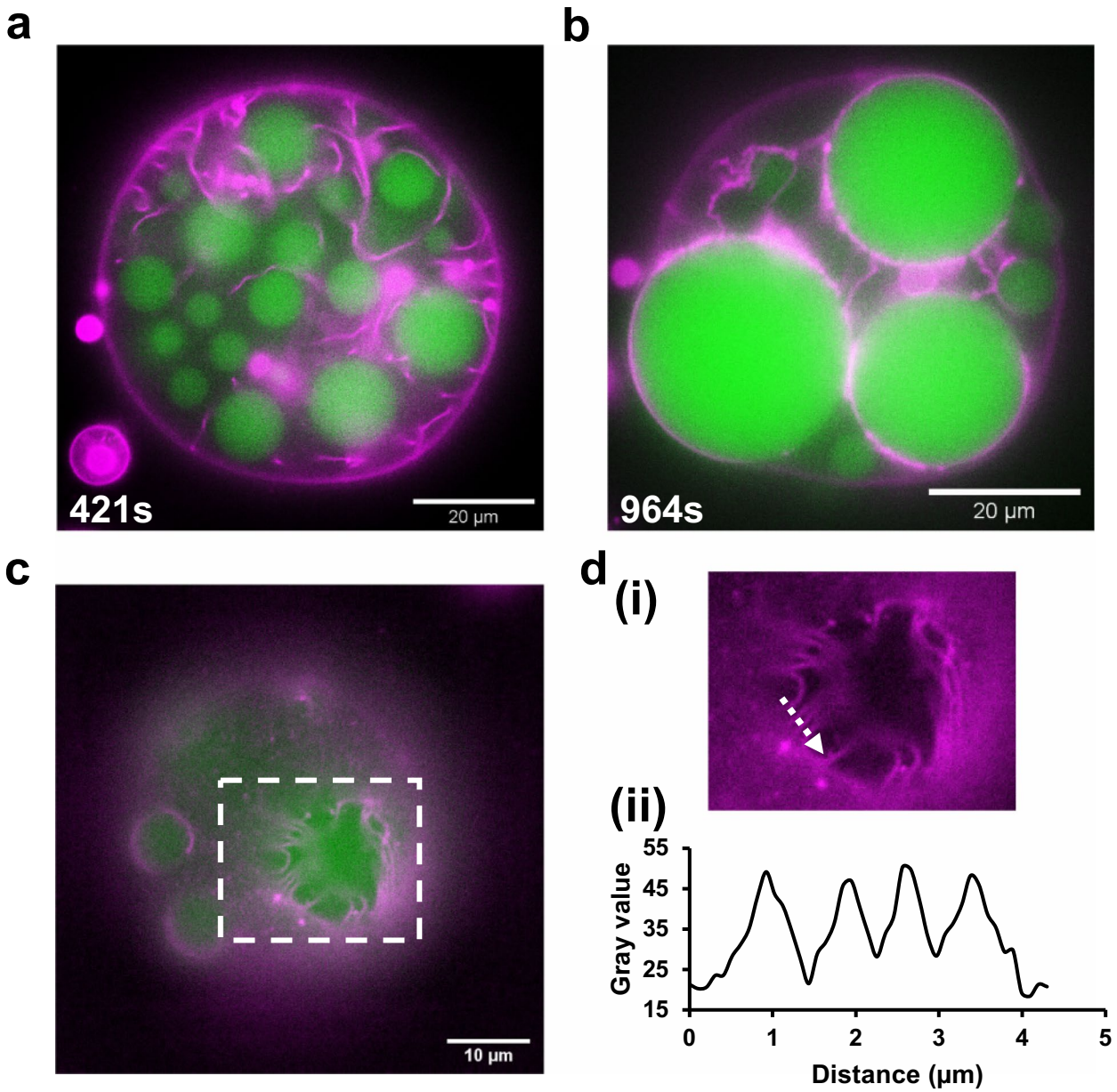

Extended Data Fig. 3 | Membrane tubule formation. (a-c) Selected frames from a time-lapse movie of wide-field fluorescence microscopy images of GUVs encapsulating a mixture of 6.0% (w/w) PEG 8 kDa and 6.4% (w/w) dextran 10 kDa doped with 0.001% AlexaFluor 488-Dextran upon immersion in 143 mM sucrose solution. (d) The plot refers to the line intensity measurement (ii) of the distance covered by the dash arrow on the adjacent image (i).

https://doi.org/10.1038/s41557-023-01267-1

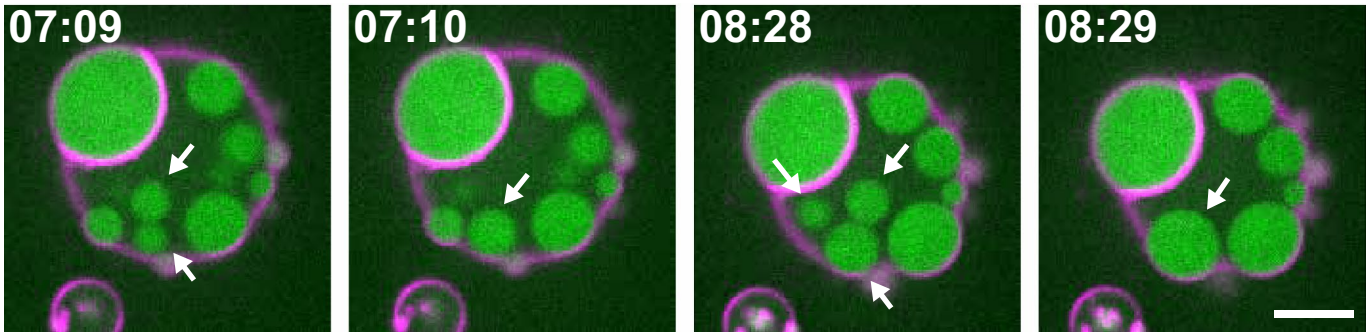

Extended Data Fig. 4 | Examples of uncoated droplets at the membrane of GUVs. Selected frames of confocal microscopy images of GUVs encapsulating a mixture of 6.0% (w/w) PEG 8 kDa and 6.4% (w/w) dextran 10 kDa doped with 0.001% AlexaFluor® 488-Dextran upon immersion in 143 mM sucrose solution. Trajectories are obtained from Supplementary Video S1. Arrows indicate examples of uncoated droplets at the membrane. All scale bar, 10 µm.

https://doi.org/10.1038/s41557-023-01267-1

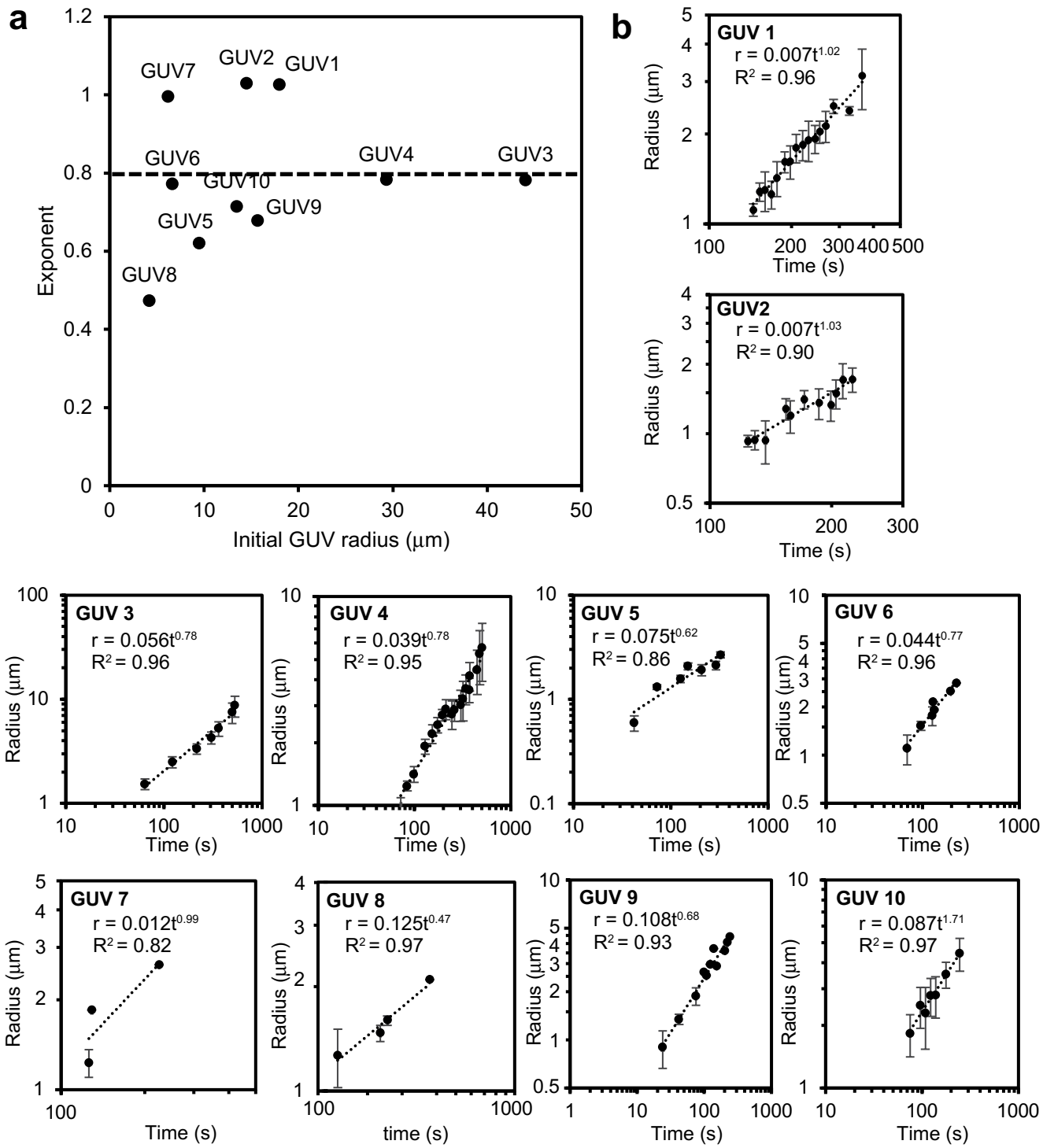

Extended Data Fig. 5 | Droplet growth analysis for GUVs of different sizes. (a) The plot shows exponent as a function of the starting GUV radius (top left, n = 10, where n refers to the number of GUV analyzed). Each data point refers to individual GUV. The droplet growth rate plots for individual GUV are also shown (b). Data are presented as mean values ± SD, (n = 10). For the number of dextran-rich droplets measured, refer to Source Data.

https://doi.org/10.1038/s41557-023-01267-1

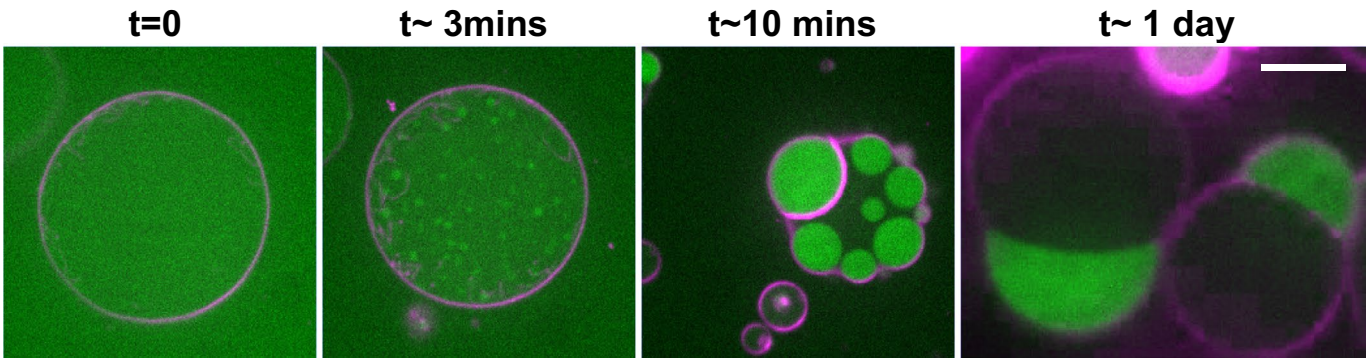

Extended Data Fig. 6 | Long-term (>24 h) follow-up of bud morphological transition. Selected frames of confocal fluorescence microscopy images of GUVs encapsulating a mixture of 6.0% (w/w) PEG 8 kDa and 6.4% (w/w) dextran 10 kDa doped with 0.001% AlexaFluor® 488-Dextran upon immersion in 143 mM sucrose solution. GUVs contain 96.8 mol% POPC, 2.2 mol% DOPE-mPEG, 1 mol% Rho-DOPE. Scale bar, 10 µm.

https://doi.org/10.1038/s41557-023-01267-1

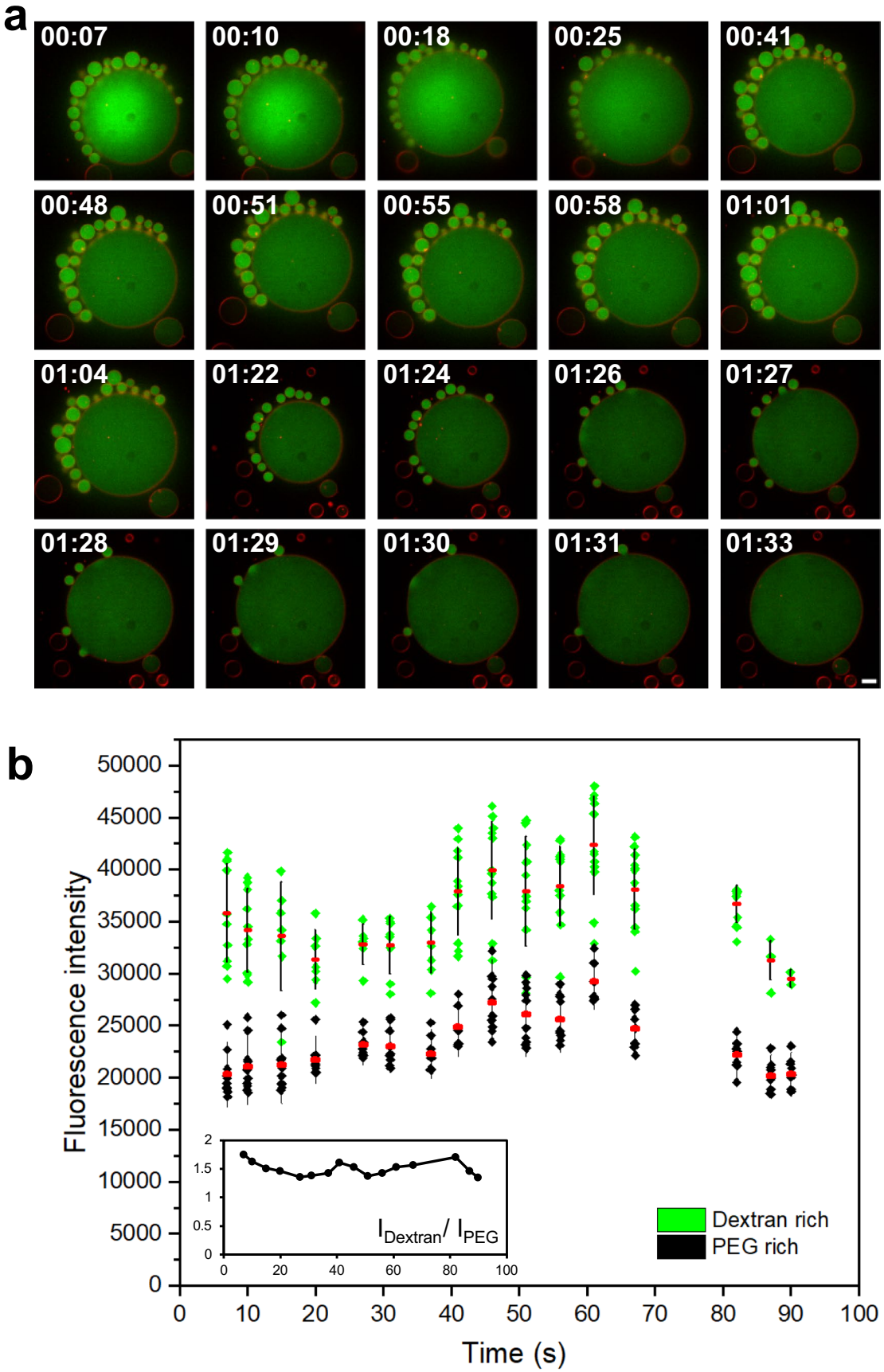

Extended Data Fig. 7 | See next page for caption.

https://doi.org/10.1038/s41557-023-01267-1

Extended Data Fig. 7 | Reversibility of osmotic deflation driven liquid-liquid phase separation. (a) Confocal fluorescence microscopy image of a single GUV consists of a mixture containing 96.8 mol% POPC, 2.2 mol% DOPE-mPEG, 1 mol% Rho-DOPE encapsulating 6.0 % (w/w) PEG 8 kDa and 6.4 % (w/w) dextran 10 kDa aqueous phase subjected to pure water (till exterior sucrose concentration equal to 62 mM) after hypertonic trigger deformation in 143 mM sucrose solution. Scale bar, 10 μm. (b) Box plot shows fluorescence intensity of individual dextran-rich droplets and PEG-rich phase as a function of time for the reversal kinetic analysis. Each data point refers to an individual measurement. The intensity values of PEG-rich phase are sampled at random spots within the GUV (n = 1). Mean values are indicated by the red dots. For the number of data points shown in the plot for each time point, refer to Source Data. The inset shows the ratio of fluorescence intensity of dextran-rich phase verses the PEG-rich phase.

https://doi.org/10.1038/s41557-023-01267-1

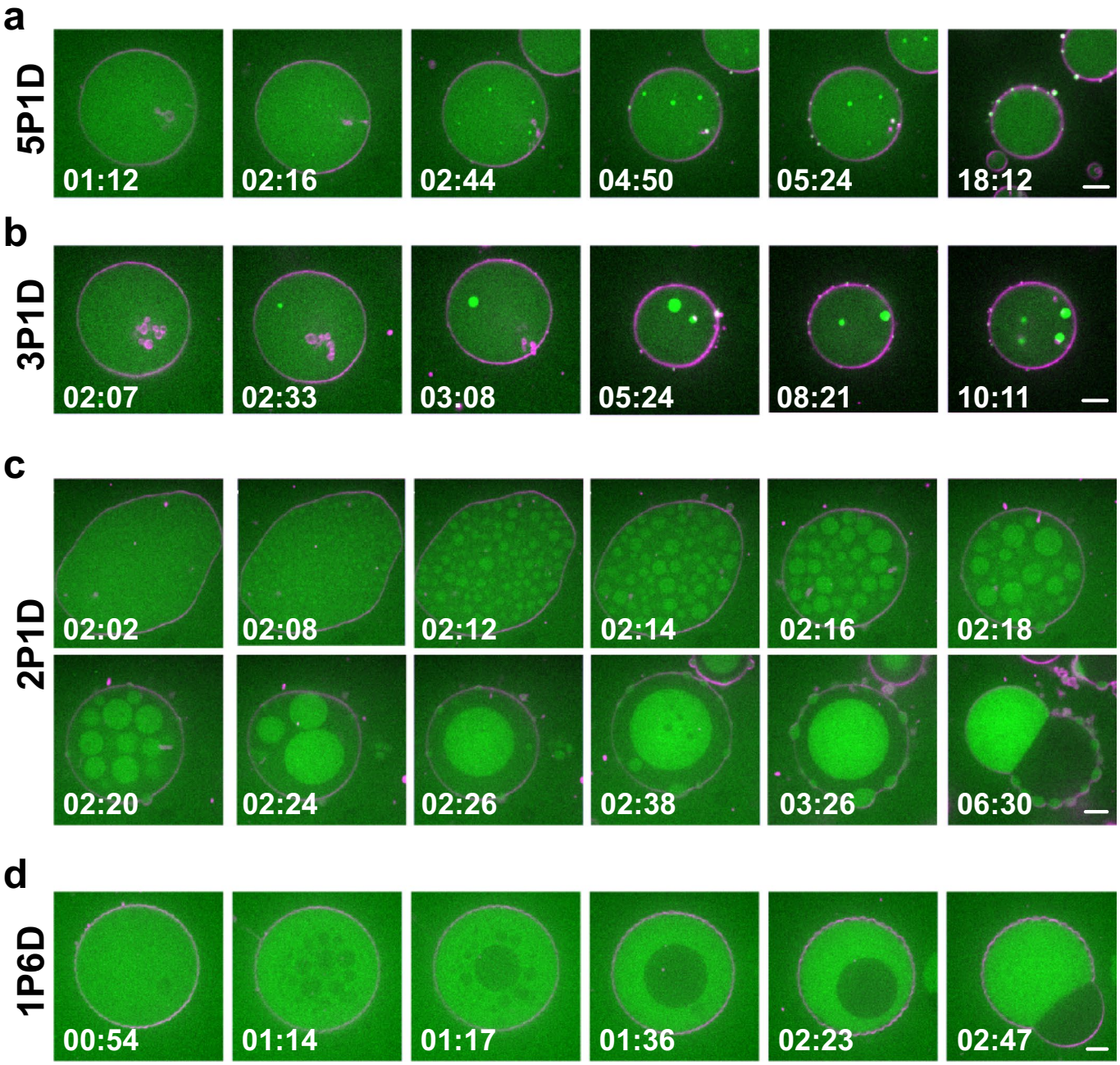

Extended Data Fig. 8 | Time-lapse confocal fluorescence microscopy image of GUVs encapsulating different LLPS mixtures. (a) 5:1 (namely 5P1D), (b) 3:1 (namely 3P1D), (c) 1:2 (namely 1P2D) and (d) 1:6 (namely 1P6D) ratios of PEG 8 kDa and dextran 10 kDa. All GUVs imaged consist of a mixture containing 96.8 mol% POPC, 2.2 mol% DOPE-mPEG, 1 mol% Rho-DOPE encapsulating PEG and dextran mixtures doped with 0.001 wt% AlexaFluor® 488 dextran upon immersion in (a) 143, (b) 120, (c) 263, and (d) 298 mM sucrose solution. All scale bar, 10 µm.

https://doi.org/10.1038/s41557-023-01267-1

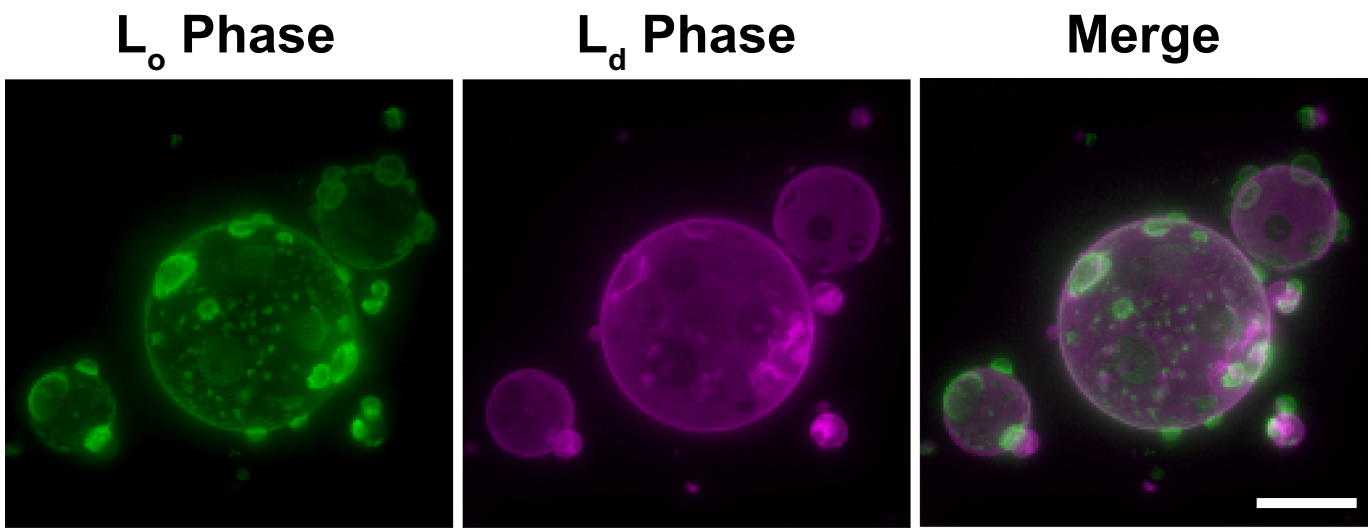

Extended Data Fig. 9 | Control GUVs without labelled dextran. The POPC: Egg-SM: Cholesterol (2:2:1) GUV, doped with 2.2% DOPE-mPEG, 1% Rho-DOPE and 3% NBD-PE with encapsulation of 6.0% (w/w) PEG 8 kDa and 6.4% (w/w) dextran 10 kDa is immersed in 143 mM sucrose solution. Scale bar: 10 μm.

https://doi.org/10.1038/s41557-023-01267-1

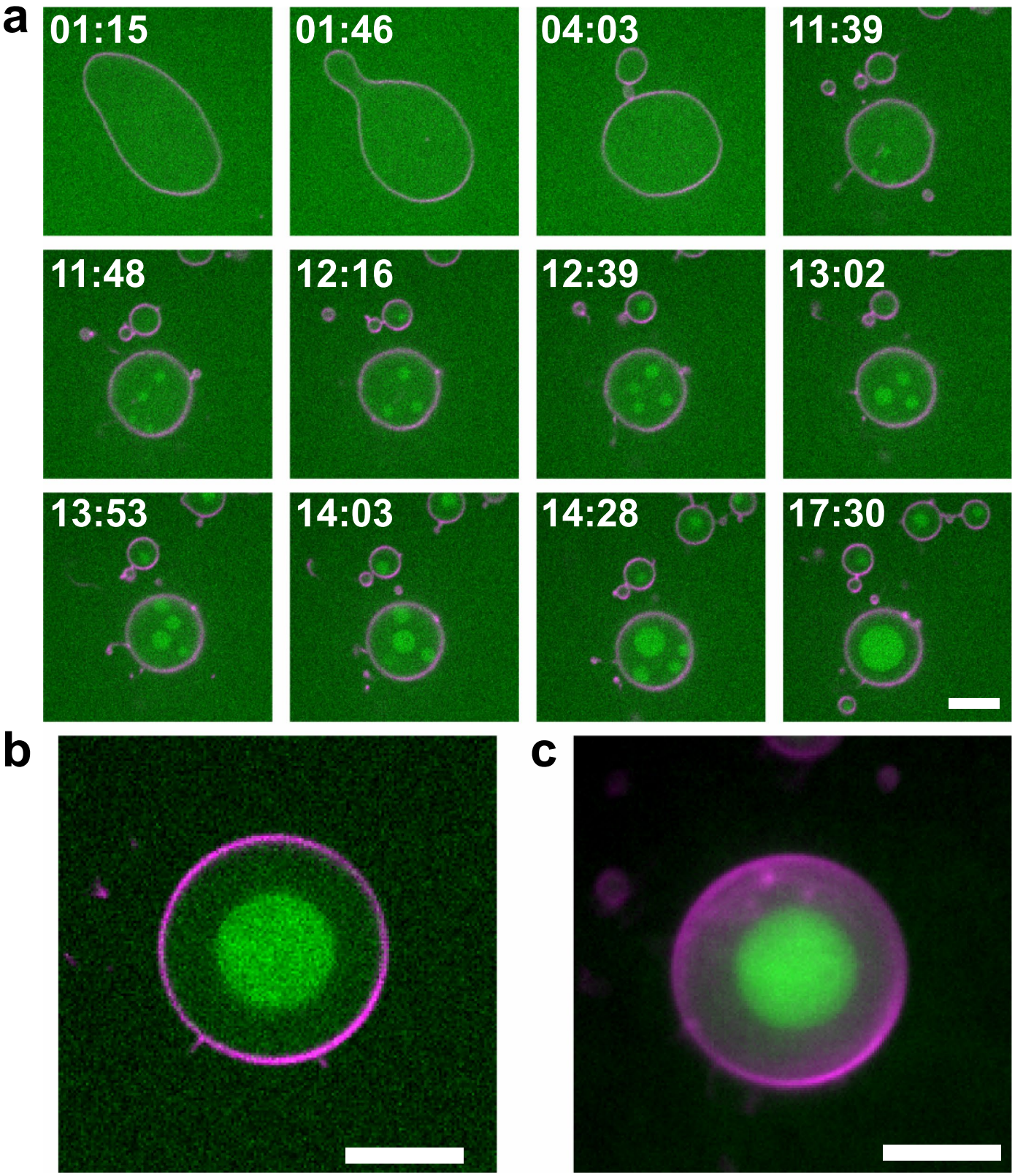

Extended Data Fig. 10 | Osmotic deflation driven LLPS in PBD-PEO GUV. (a) Selected frames from a time-lapse video of 99 % PBD-PEO GUV doped with 1% Rhodamine-DOPE, encapsulating a mixture of 6.0% (w/w) PEG 8 kDa and 6.4% (w/w) dextran 10 kDa doped with 0.001% AlexaFluor® 488-Dextran upon immersion in 143 mM sucrose. Confocal section (b) and 3D projection (c) of the final morphology are shown. All scale bar, 10 µm.